広島大学 学位論文

Photoluminescence Properties of Distorted Titanates Investigated by X-ray Absorption Spectroscopy

X線吸収分光法による歪んだチタン酸化物のフォトルミネセンスの研究

2020 年

広島大学大学院理学研究科
物理科学専攻

Dongxiao Fan

目次

- **主論文**

  Photoluminescence Properties of Distorted Titanates Investigated by X-ray Absorption Spectroscopy

  Ｘ線吸収分光法による歪んだチタン酸化物のフォトルミネセンスの研究

  Dongxiao Fan

- **公表論文**

  Photoluminescence mechanism of self-activated titanate phosphors investigated by X-ray absorption spectroscopy under UV irradiation

  Dongxiao Fan, Nobuo Nakajima, and Seiya Kato

  Journal of Physics: Condensed Matter, 2020.

- **参考論文**

1. **Enhanced afterglow property of $BaAl_2O_4$: Eu^{2+}, Dy^{3+} phosphors by adding Li_2CO_3.**

   Ma, Junfeng, **Dongxiao Fan**, Bingbing Niu, Xuena Lan.

   Functional Materials Letters, 10(03), 1750020 (2017).

2. **The in situ growth of 3D net-like CNTs on C fiber.**

   Junfeng Ma, Xuena Lan, Bingbing Niu, **Dongxiao Fan**.

   Materials Chemistry and Physics, 192, 210-214 (2017).

主論文

• Abstract

Titanium–oxygen polyhedra, such as TiO_4 with a tetrahedron structure, TiO_5 with a square pyramidal structure, and TiO_6 with an octahedron structure, commonly exist in titanate materials from the perspective of microscopic scale. The physical properties of titanates greatly depend on the local structure of titanium–oxygen polyhedra. For example, Ba_2TiO_4, which contains a series of isolated TiO_4 tetrahedra, has excellent CO_2 sorption properties. Fresnoite structure materials containing TiO_5 polyhedron exhibit strong second harmonic generation response and have been widely used in second-order nonlinear optical materials. The TiO_6 octahedron is more well-known than TiO_4 and TiO_5; further, it is contained in titanates with perovskite structure, which is currently a research hotspot. A typical example of physical property related with TiO_6 octahedron is the ferroelectricity in $BaTiO_3$ and $PbTiO_3$, which is produced by the displacement of a titanium ion in an octahedron cage. In terms of structural similarity, TiO_5 can be considered to be resulting from the TiO_6 octahedron with Ti ion displacement along the z-axis. The local structural characteristics of these polyhedra in materials contribute to their physical properties.

Self-activated titanate phosphors with TiO_5 polyhedra exhibit excellent photon-emission property under UV irradiation, i.e., photoluminescence (PL). This phenomenon is also observed in $BaTiO_3$ with distorted TiO_6 octahedron. Interestingly, both PL and ferroelectric properties result from the distortion of TiO_6 octahedron. The term "self-activated phosphors" is assigned to non-ion-doped phosphors, whereas conventional phosphors are created by doping ions in a matrix as the color center. The function of the doped ions is to form in-gap states. To determine the role of the TiO_5 polyhedron in self-activated titanate phosphors, the local electronic states in the TiO_5 polyhedron must be investigated. The incipient ferroelectric material $SrTiO_3$, which is known to be centrosymmetric over the entire temperature range, also exhibits PL with faint blue light emission at temperatures less than 37 K. This fact motivated us to investigate the local structure of TiO_6 based on the influence of temperature and UV irradiation. Further, for clarifying the reports about the appearance of dipole moment and the increase in dielectric constant of $SrTiO_3$ under UV irradiation, the local structure information is required. Due to its sensitivity to specific atomic species and the high

resolution of spatial distribution, X-ray absorption fine structure (XAFS) is an ideal approach for investigating the electronic states of self-activated phosphors and the local structure of $SrTiO_3$ under UV irradiation.

The Ti K-edge X-ray absorption near edge structure of self-activated titanate phosphors ($Ba_2TiSi_2O_8$, $Sr_2TiSi_2O_8$, and Na_2TiSiO_5) were analyzed with UV irradiation, from which two features in the pre-edge region were observed: a large pre-edge feature and a hump. The electronic states of the features are determined by theoretical calculations. The electronic states of the pre-edge, which originate from the hybridization of Ti $3d$, Ti $4p$, and O $2p$, act as in-gap states to emit visible light in the PL process. The electronic state of the hump, which originates from the sub-band of Ti $4p$, acts as an electron trap for the electrons excited by UV irradiation. These results confirm the color center nature of TiO_5 polyhedron. An energy diagram of self-activated titanate phosphors was proposed to clarify the PL property.

To investigate the local structure that is advantageous to realize the PL property, a Ti K-edge extended XAFS of $SrTiO_3$ was performed at 22–300 K under UV irradiation. By using the tetragonal structure model of $SrTiO_3$ to fit the data, the dynamic Ti ion displacement along the z-axis is confirmed, which illustrates the instantaneous existence of TiO_5 polyhedron. With UV irradiation, the Ti ion vibration along the z-axis is significantly enhanced, which explains the appearance of dipole moment and the increase in the dielectric constant of $SrTiO_3$.

The in-gap states are necessary to produce the PL property in non-ion-doped titanates. Moreover, the TiO_5 polyhedron can create in-gap states. The distortion of TiO_6 octahedron in $SrTiO_3$ results in TiO_5 polyhedron. Therefore, the PL property can be adopted as an effective characterization method to investigate the in-gap electronic states and determine the local structure distortion in non-ion-doped titanates. The simultaneous existence of PL and the ferroelectric property caused by the local structure distortion reveal a new direction for investigating new multifunctional materials.

Contents

1 Introduction

1.1 Basic characteristics

Titanate materials play an important role in the field of modern condensed matter physics. Various types of titanate compounds exhibit excellent and diverse physical properties, such as photocatalysis, ferroelectrics, photoluminescence, and surperconductivity [1–4]. Titanate oxides have been most popular since the discovery of ferroelectricity in perovskite-type oxides (e.g., $BaTiO_3$) in the first half of the 20th century. In 1972, the report on photochemical catalysis of TiO_2 by Fujishima significantly expanded the research on titanate materials and their potential for practical applications. Currently, utilizing advanced techniques such as sample preparation and characterization to explore the novel physical functional properties and investigate the profound physical mechanisms behind the physical phenomena has become very common.

The defining factor of the physical properties of any material is its constitutive structure. The image of materials science tetrahedron (figure 1-1), which concisely depicts the relationship of interdependence between the structure, properties, performance, and processing, shows that the structure of materials occupies the irreplaceable top position and contacts all the other terms [5]. In terms of scale, the structure of the material is of two types, namely, macroscopic structure and microscopic structure; the macroscopic structure is average results of microscopic structure. For example, the conventional interpretation of ferroelectricity in perovskite-type titanates is Ti ion displacement from the symmetric center, whereas the ferroelectricity in $BaTiO_3$ along the [001] direction in the macroscopic scale is an average result of the Ti ion displacement along the [111] direction in the microscopic scale [6]. In addition, the microscopic structure of a material can strongly influence the physical properties such as strength, toughness, ductility, hardness, corrosion resistance, high- or low-temperature behavior, and wear resistance [7]. Therefore, revealing the local structure of a material can significantly enhance the understanding of its physical properties. Generally, the macroscopic structure of a specific material can be measured by conventional X-ray diffraction (XRD) and Raman spectroscopy, which are sensitive to the long-range order of the materials. For

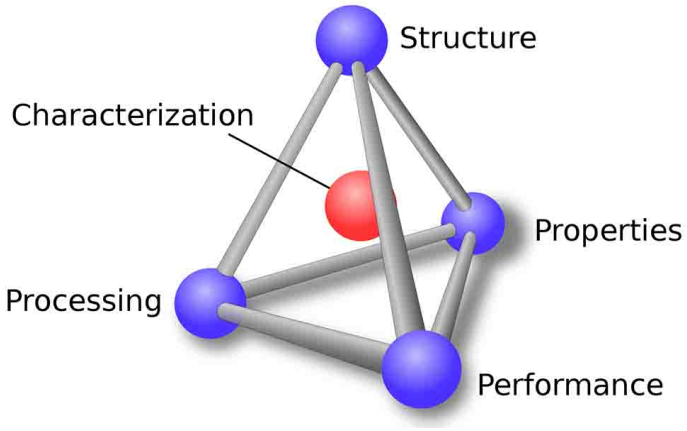

Figure 1-1: Schematic of materials science tetrahedron.

the microscopic structure, such as chemical bond distance, coordination number, and the symmetric property, X-ray absorption fine structure (XAFS) is an ideal approach for probing these local structures because of its characteristics of high resolution of the spatial distribution of atoms and sensitivity to specific atomic species and local structures [8, 9].

1.2 Titanium–Oxygen polyhedra

In terms of the local structure of titanate compounds, three types of titanium oxygen polyhedra are available: TiO_4 with tetrahedral structure, TiO_5 with a square pyramidal structure, and TiO_6 with octahedral structure (figure 1-2). The different local structures result in distinct physical properties on the macroscopic scale, and determine the practical applications in daily life. For example, Ba_2TiO_4, which contains a series of isolated TiO_4 tetrahedra, has excellent CO_2 sorption property and can be used for improving the air qualities [10]. TiO_5 polyhedron, which is present in materials with fresnoite structure because of the existence of the short Ti–O between the apical O and central Ti, exhibits strong second harmonic generation response, and has been widely used for second-order nonlinear optical materials [11]. TiO_6 is not only a more common titanium–oxygen polyhedron among the titanate compounds such as TiO_4 and TiO_5, but also commonly exists in perovskite-type titanates. Tremendous physical properties are associated with the TiO_6 octahedron local structure. Specifically, in the field of titanate ferroelectric materials, ferroelectricity is produced

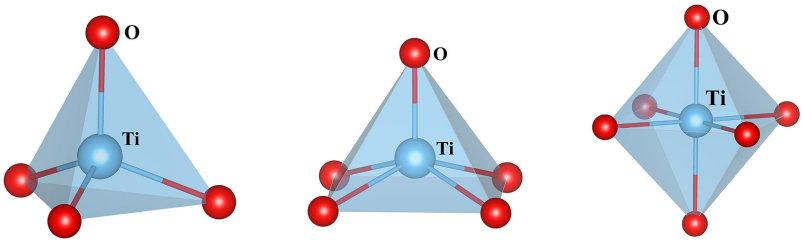

(a) TiO_4 (b) TiO_5 (c) TiO_6

Figure 1-2: Structures of various titanium–oxygen polyhedra: (a) tetrahedral TiO_4, (b) square pyramidal TiO_5, (c) and octahedral TiO_6.

by the displacement of titanium ions in an octahedron cage, such as $BaTiO_3$ and $PaTiO_3$ [2]. Further, another distortion of TiO_6 octahedron is also available, which is the rotation of the oxygen octahedron without Ti displacement. Because the centrosymmetry is not broken during this rotation, no ferroelectricity is realized.

In the case of isolated Ti atoms, the $3d$ orbitals are five-fold degenerate with an equivalent energy level (figure 1-3 (a)). In perovskite titanates, because a Ti ion is located at the center of the octahedron, Ti^{4+} experiences an octahedral field with O_h symmetry. Based on the ligand field theory, the five-fold degenerated $3d$ orbitals of a Ti ion with O_h symmetry will be split into a triply degenerated t_{2g} (d_{xy}, d_{yz}, and d_{xz}) energy level and a doubly-degenerated e_g ($d_{x^2-y^2}$ and d_{z^2}) energy level, in which the energy level of e_g is higher than that of t_{2g}. However, in a tetrahedral field, the order of energy level is reversed and the magnitude of splitting is less [12], as shown in Figure 1-3 (b). In the case of $3d$ orbitals in the TiO_5 polyhedron, because the symmetry breaks along the horizontal plane, the splitting of energy levels becomes more complicated.

Considering the local characteristic nature of titanium–oxygen polyhedra, XAFS is adopted as the common experimental approach to detect the electronic states and the local atomic arrangement structure. It is well-known that the pre-edge of X-ray absorption spectroscopy (XAS) is related to the electronic transition from the core level to the unoccupied electronic states of the conduction band; therefore, the pre-edge feature can provide useful electronic information. Figure 1-4 shows the pre-edge of Ti K-edge XAS of strontium titanate ($SrTiO_3$

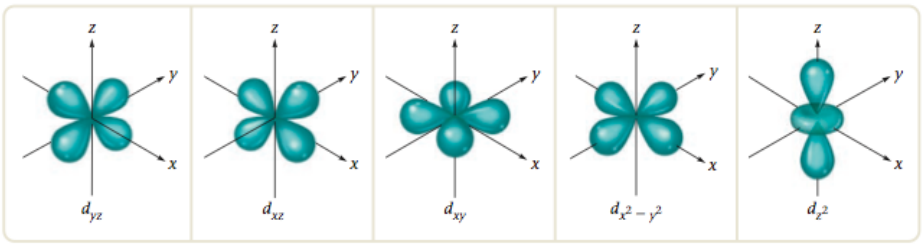

(a) $3d$ electron orbitals of isolated atoms

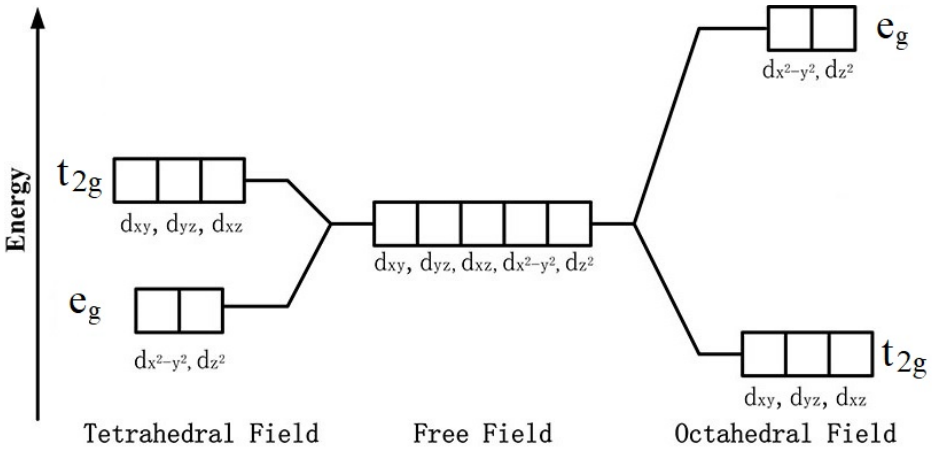

(b) $3d$ electronic orbitals under free, tetrahedral, and octahedral fields

Figure 1-3: Schematic of (a) $3d$ electron orbitals of isolated atoms, and (b) crystal-field splitting of $3d$ electronic orbitals under different fields.

or STO). There are three peaks marked as A_1, A_2, and A_3 in the pre-edge. The A_1 peak is corresponding to the Ti $1s$ to the t_{2g} electronic transition and the A_2 is corresponding to the Ti $1s$ to the e_g electronic transition. Because of the $3d$-type nature of t_{2g} and e_g, both transition belong to the quadrupole transition. The electronic state of A_3 peak originates from the inter-atomic hybridization from $3d$ orbital of the absorbing Ti and the $4p$ of the neighboring Ti, so A_3 peak is corresponding to the dipole transition. Therefore, the information of electronic states and transition type can be obtained from the XAS experiment. The electronic states are sensitive to the symmetry property of the absorbing atom, so XAS experiment can also probe the microscopic structure of the materials. Thus, the sensitivity of XAS to the local structure makes it a suitable technique for studying the local structure of titanate compounds.

Two types of titanium–oxygen polyhedra containing materials are studied in this thesis.

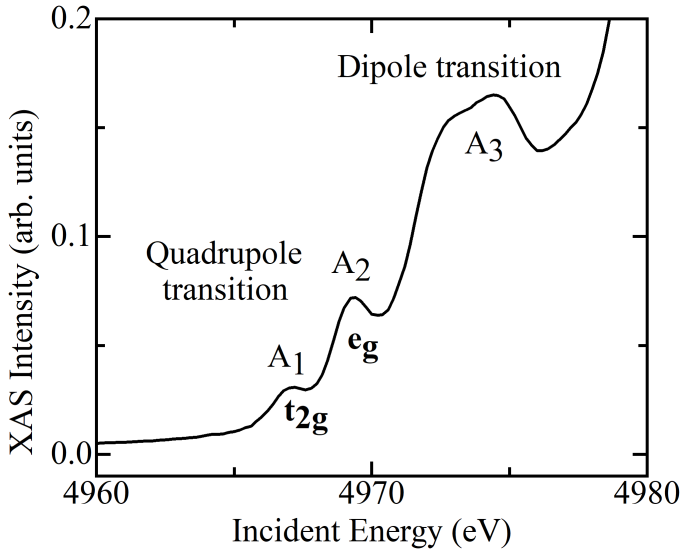

Figure 1-4: The pre-edge of Ti K-edge XAS of $SrTiO_3$.

One is TiO_5 polyhedron containing titanates, which exhibit intense photoluminescence (PL) under UV irradiation. Because these titanate phosphors do not contain dopants to act as color centers, they can be termed as self-activated titanate phosphors. The materials belonging to the fresnoite family with intrinsic square pyramidal TiO_5 polyhedron, $Ba_2TiSi_2O_8$ (BTSO), $Sr_2TiSi_2O_8$ (STSO), and Na_2TiSiO_5 (NTSO) are typical self-activated titanate phosphors, and can emit intense visible light under UV irradiation. The TiO_5 polyhedron structure plays a crucial role in the PL process. To understand the PL mechanism of these self-activated titanate phosphors, the electronic states around the valence band are required. The electronic states formed by the TiO_5 polyhedron are studied by X-ray absorption near edge structure (XANES). The other material is $SrTiO_3$ containing TiO_6 octahedron. $SrTiO_3$ exhibits various physical responses to UV stimulation. At room temperature, cubic $SrTiO_3$ does not possess the PL property; however, once the TiO_6 octahedron in $SrTiO_3$ becomes distorted, $SrTiO_3$ exhibits faint emission under UV irradiation [13]. Furthermore, $SrTiO_3$ exhibits PL at low temperatures of less than 37 K [14]. Because $SrTiO_3$ maintains centrosymmetry over the entire temperature range, as observed from the XRD results, no substantial distortion exists in the TiO_6 octahedron; consequently, no PL should occur. Some studies have reported that the Ti ion movement along the [001] direction in $SrTiO_3$ can be excited under UV irradiation, which will form the TiO_5 polyhedron [15]. This phenomenon has a significant importance

in investigating ferroelectricity in $SrTiO_3$. However, Ti ion motion under UV irradiation has not been proved experimentally. Therefore, the local structure of $SrTiO_3$ is investigated by XAFS.

1.3 TiO_5 polyhedron containing self-activated titanate phosphors

Photoluminescent materials have wide practical application prospects, such as lighting, photosensitive detectors, cathode ray tubes, bioimaging, and decoration [16–18]. Generally, photoluminescent materials are obtained by doping ions in a host matrix. The doped ions serve as color centers, and the host matrix provides a suitable crystal field environment. The doped ions can create in-gap states between the valence band and the conduction band. The electrons in the valence band can be excited to the conduction band by UV irradiation. The excited electrons undergo energy and momentum relaxation toward the in-gap states. Visible light with longer wavelength compared with UV light will be emitted after the electron jump back the band gap minimum (Figure 1-5). During the PL process, the in-gap states play an important role in inducing the emission of visible light. Because rare earth elements contain abundant electronic energy levels and exhibit bright emission intensity and high quantum conversion efficiency, rare-earth ion-doped photoluminescent materials have been most widely utilized in light-emitting materials in the past few decades. However, due to limited availability and the continuously increasing cost of rare-earth elements, it is necessary to find appropriate alternatives for rare-earth ion-doped phosphors. Non-doped titanate materials with good photoluminescent property are garnering increasing attention owing to their advantages of high emission intensity, wide emission band, and rare-earth-free nature [19].

Generally, titanate compounds with high crystal symmetry have wide energy gaps, e.g., 3.3 eV for tetragonal $BaTiO_3$ (space group P4mm) and 3.4 eV for cubic $SrTiO_3$ ($Pm\bar{3}m$), and do not exhibit PL. If the structures are distorted, these perovskite titanates exhibit PL under UV irradiation [13, 20]. The distortion of the TiO_6 octahedron is shown in figure 1-6. After the distortion, the linkage of adjacent TiO_6 octahedron along the z-axis is broken. Further, because a square pyramidal titanium–oxygen polyhedron TiO_5 is produced, the

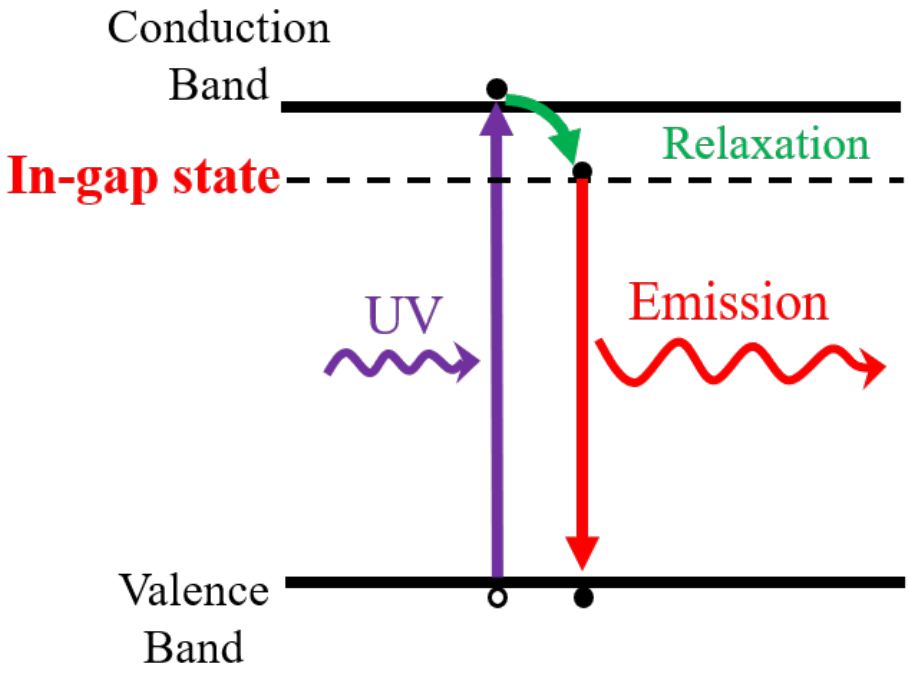

Figure 1-5: Energy diagram of the photoluminescence process

TiO_5 polyhedron can be regarded as a distorted TiO_6 octahedron. During distortion, the symmetry of the octahedron is reduced, and the energy levels of e_g and t_{2g} will be further split [21], resulting in the creation of in-gap states. The creation of in-gap states causes the PL phenomenon in the distorted perovskite titanates. Therefore, the existence of TiO_5 polyhedron is indispensable for producing the PL property.

Many TiO_5 polyhedron containing titanate compounds exhibit PL. Table 1-1 lists some self-activated phosphors containing TiO_5 polyhedron with different excitations and emission wavelengths; among these, the white-light-emitting phosphors are more interesting than the others. In recent years, the application of white-light-emitting rare-earth-free phosphors in white-light-emitting diodes has received considerable attention because of their high brightness, low energy consumption, and environment-friendly property. Moreover, they can be used in field-emission displays, thereby realizing displays with thin panels, wide viewing angle, fast response time, high contrast ratio, and low power consumption. Many oxide compounds containing transition metal ions coordination polyhedron with d^0 electron configurations such

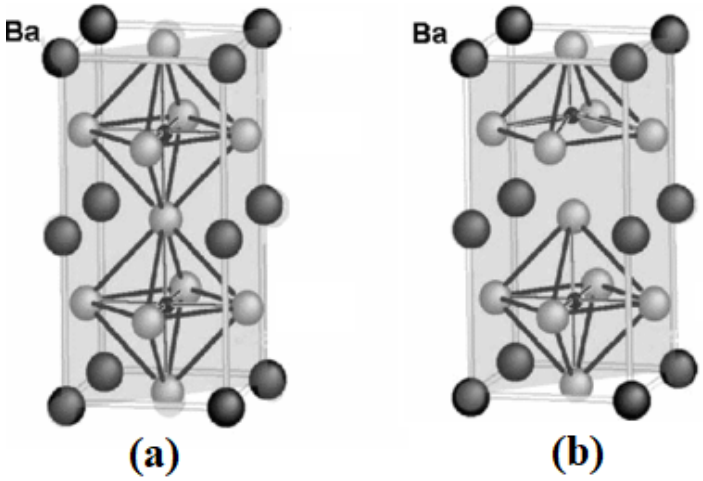

Figure 1-6: Lattice structure of $BaTiO_3$ with (a) O_h symmetry TiO_6 octahedron and (b) distorted octahedron TiO_5 [20].

as Ti^{4+}, V^{5+}, and W^{6+} have shown good white light emission intensity under UV irradiation. Among such closed-shell transition metal containing phosphors, titanate phosphors have been more extensively studied because of their advantageous optical properties; furthermore, these materials are used as tunable solid-state laser hosts, nonlinear optical materials, phosphors, and long-lasting phosphorescence materials. All these benefits make titanate phosphors more advantageous than the other rare-earth-free phosphors.

It is well-known that Ti^{4+} ions-doped or –containing materials exhibit blue and yellow emission under UV irradiation. The blue emission is caused by the charge-transfer transition from $2p$ orbits of O^{2-} to $3d$ orbits of Ti^{4+}, i.e., O^{2-}-Ti^{4+} $\rightarrow$ O^{-}-Ti^{3+}, whereas the yellow emission results from the titanium octahedron associated with oxygen defects [3]. In the case of self-activated titanate phosphors, because there are no doping ions to act as color centers in which electron excitation and de-excitation occur, the color responsible for the PL property is unclear. The methods for producing in-gap states differ between rare-earth-doped phosphors and self-activated titanate phosphors; therefore, the electronic states and the microscopic structure of self-activated titanate phosphors essential for realizing the photoluminescent phenomenon should be different. It has been reported that a single short Ti–O bond in a TiO_5 polyhedron is essential for PL [22], but this theory has not been studied in detail. Although

Table 1-1: Various TiO_5 polyhedron containing self-activated titanate phosphors and their PL properties.

Titanate phosphors	Wavelength (Ex.) (nm)	Wavelength (Em.) (nm)	ref
$Ba_2TiSi_2O_8$	260	450	[23]
$Sr_2TiSi_2O_8$	260	492	[24]
Na_2TiSiO_5	250	460	[3]
$Ba_2TiP_2O_9$	254	490	[25]
Li_2TiSiO_5	250	505	[26]
$LiTiPO_5$	254	490	[26]
Na_2TiGeO_5	255	425	[27]

the electronic states have been evaluated using the Raman spectroscopy data in previous works, there are no reports that correlate the in-gap states and the orbital characteristics of the relevant atoms. Thus, the electronic states of self-activated titanate phosphors are investigated via UV irradiation.

To investigate the electronic states essential for realizing the PL property in self-activated titanate phosphors, an appropriate technique must be used. As discussed above, XANES has the advantageous characteristics of high resolution in measuring the electronic states around the valence band, and is sensitive to particular atomic species and local structures [8, 9]. The origin of XANES is the transition of the Ti $1s$ electrons to the unoccupied electrons states near the bottom of the conduction band. Because the conduction band mainly originates from the vacant $3d$ atomic orbitals of the Ti atoms in the compound, the lowest conduction band can be a battle field for UV and X-ray excited electrons. Thus, XANES is an ideal technique for studying the photoluminescent phenomenon of self-activated phosphors. The doping ratio of ion-doped phosphors is only several percentage or less, detecting which is difficult using XANES.

1.4 TiO_6 Octahedron distortion in $SrTiO_3$

Perovskite-type $SrTiO_3$ has perfect cubic structure at room temperature and undergoes an antiferrodistortive phase transition at 105 K, which is the rotation of the TiO_6 octahedron along the z-axis [28]. An Sr subunit cell of $SrTiO_3$ with two phases is shown in Figure 1-7. Despite undergoing phase transition, the stability of the centrosymmetry within the entire temperature range makes $SrTiO_3$ a very stable structure. $SrTiO_3$ has the space group $Pm3m$ with 3.905 Å lattice constant at room temperature and $I4/mcm$ space group at low temperatures.

$SrTiO_3$ possesses several excellent physical characteristics such as high thermostability and chemical stability, large dielectric constant, photocatalysis, superconductivity, and sensitivity to external stimulation such as pressure or photon. [29, 30]. $SrTiO_3$ is a typical incipient ferroelectric material and has quantum paraelectricity below 37 K [31]. With decreasing temperature, the dielectric constant increases gradually, but the ferroelectric phase never appears, which is a result of quantum fluctuations and the antiferrodistortive phase transition at low temperature [32]. Nevertheless, various physical approaches have been used to obtain ferroelectricity in $SrTiO_3$ in the macroscopic scale even at room temperature, such as ion doping, isotropic exchange, strain performance, low dimension treatment, and coherent motive modulation [33–37].

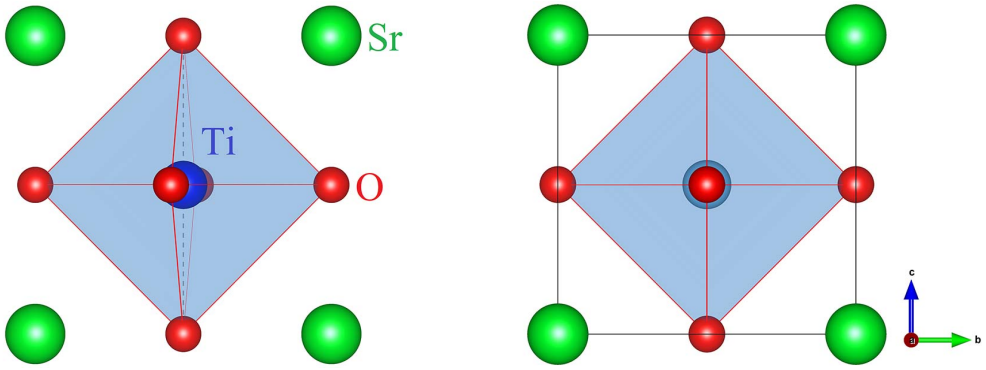

(a) (b)

Figure 1-7: Sr subunit cell of $SrTiO_3$: (a) tetragonal structure and (b) cubic structure; the rotation of the TiO_6 octahedron in (a) corresponds to antiferrodistortive phase transition.

As discussed above, cubic $SrTiO_3$ do not exhibit PL, and only the distorted $SrTiO_3$ shows faint emission under UV irradiation. However, $SrTiO_3$ exhibits PL below 37 K (Figure 1-8), which has an important significance in investigating new physical properties of $SrTiO_3$ [14]. Because $SrTiO_3$ maintains centrosymmetry over the entire temperature range, as revealed by XRD results, no large distortion exists in the TiO_6 octahedron; thus, no PL should occur. With the statement in the last section, the existence of TiO_5 polyhedron is very important for the PL property of self-activated titanate phosphors. The TiO_5 square pyramid is frequently considered as the Ti ion displacement from the octahedral center along the *c*-axis. In addition, the point group of the distorted TiO_6 by the way of Ti ion displacement is C_{4v}, which is same as the TiO_5. It is reasonable to suspect that small distortion of the TiO_6 in $SrTiO_3$ exist to produce the PL property. To resolve this problem, the local structure of TiO_6 in $SrTiO_3$ must be investigated. Because the UV irradiation is the necessary for the PL property, the technique used for the detection must be available to combine the UV irradiation.

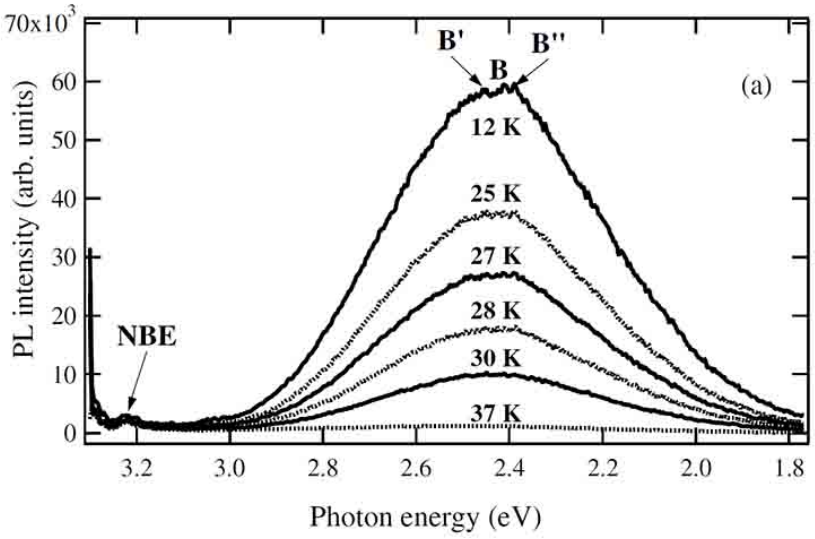

Figure 1-8: Photon emission spectra of $SrTiO_3$ at less than 37 K; no PL property appears at high temperatures [14].

Various methods have been reported to detect the distortion of the TiO_6 octahedron related with the off-center Ti ion in the octahedral cage. The conventional techniques of

XRD and Raman can provide local structure information about the average positions of the atoms in the crystal lattice. Thus, they are not suitable to detect the microstructure of $SrTiO_3$. One of the reports about the Ti displacement in cubic $SrTiO_3$ was measured by nuclear magnetic resonance spectroscopy (NMR). A model of eight off-center displacements along with the eight [111] direction in $SrTiO_3$ was proposed (figure 1-9). In this model, the Ti displacement caused by the soft mode combined with the 8-site order-disorder model gave a good agreement with the experiment data [38]. However, the NMR technique is difficult to combine the UV irradiation.

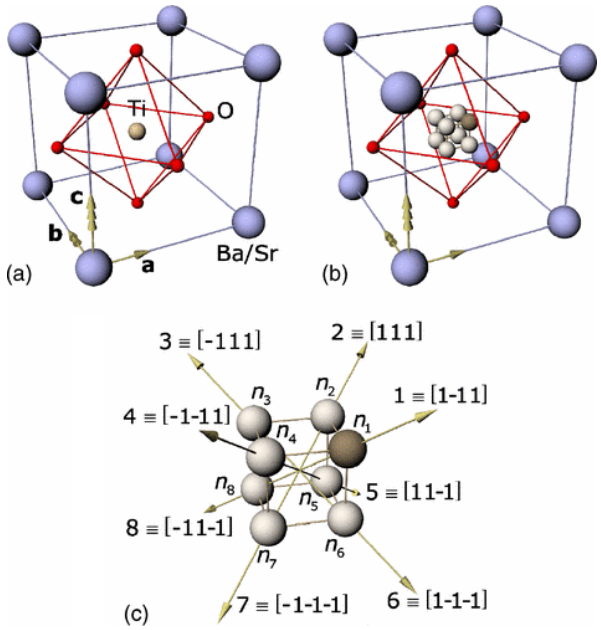

Figure 1-9: Intrinsic Ti disordered along the eight [111] directions off-center displacements [38].

On the microscopic scale, XAFS is one of the best techniques to detect Ti displacement. It is well-known that the intensity of the pre-edge of Ti K-edge XANES is a good indicator of the appearance of Ti ion displacement. In addition, extended X-ray absorption fine-structure spectroscopy (EXAFS) can directly measure the magnitude of Ti ion displacement in perovskite materials. The quasiamorphous phases of $SrTiO_3$ do not show macroscopic scale polarization, but both XANES and EXAFS results reveal clear Ti displacement in quasiamorphous $SrTiO_3$ (Figure 1-10) [39]. It is interesting that the Ti K pre-edge XANES has some intensity even for the crystalline cubic $SrTiO_3$, which indicates that the Ti displacement in cubic $SrTiO_3$ may exist. This assumption has been verified by the EXAFS results [40], which have shown that the displacement value is approximately 0.1 Å. However, the quality of data in this report is not good. Generally, the longer of the data range in k-space, more precise of the measurement can be obtained for the distance between the atoms. In this report, only k range (2.5 to 9 $Å^{-1}$) was used. The direct consequence of this shorted data is that only one peak (Ti-Ti) appears, the peak of Ti-Sr is overlapped in the Ti-Ti peak, which will reduce the accuracy of the measurement. In my present study, more long k range data were obtained with more higher resolution in energy.

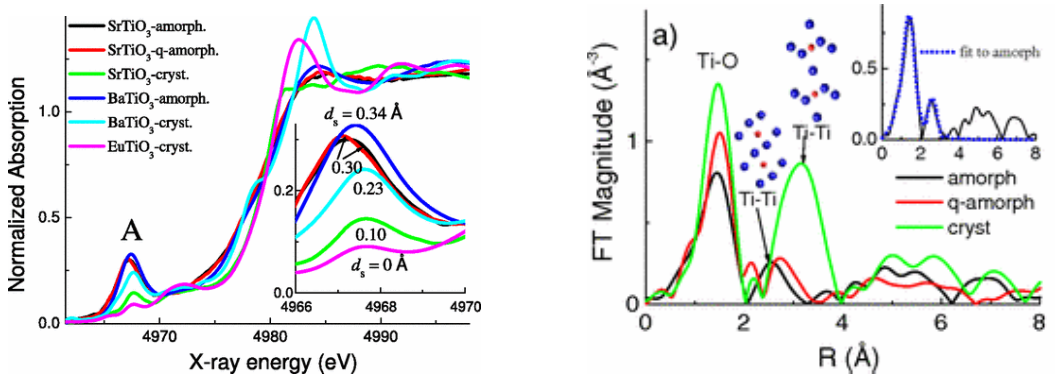

(a) (b)

Figure 1-10: (a) Ti K-edge XANES spectra of crystalline, amorphous and quasiamorphous $SrTiO_3$, and (b) magnitudes of Fourier transforms of the k^2-weighted EXAFS spectra for crystalline, amorphous, and quasiamorphous $SrTiO_3$ [39].

The advantage of EXAFS is not only the sensitivity of the local structure and atomic species, but also the time scale. The lifetime of an excited state in XAFS is in the order of femtoseconds, which far exceeds the periodic time of atomic vibration and the fluorescence decay time of PL. Therefore, EXAFS is suitable for detecting the influence of UV on $SrTiO_3$.

The meaning of the measurement for the displacement of Ti ion off center is not limited at revealing the origin of the PL property of $SrTiO_3$. It also can explained other physical phenomenon of $SrTiO_3$ related with the UV stimulation. A prominent physical property of $SrTiO_3$ is photosensitivity. Takesada reported a drastic increase in the dielectric constant of quantum paraelectric $SrTiO_3$ under UV irradiation and weak DC Electric Field (Figure 1-11) [41]. The influence of UV on the dielectric constant indicates that UV can affect the local structure of $SrTiO_3$. It is considered that the enhancement of the dielectric constant is caused by the photoinduced polar domain. However, this conclusion is controversial, because after the UV irradiation, the electrons in valence band can be excited to the conduction bands, the electron migration in the conduction band can cause the leakage of electric current between the electrode during the measurement, which can also increase the value of measured dielectric constant. Nozawa investigated this phenomenon using XANES and found an enhancement of the pre-edge, which is considered as the vibration of Ti ions along the z-axis (Figure 1-12) [15, 42]. However, no experiments have been conducted to measure the vibration of Ti ions directly.

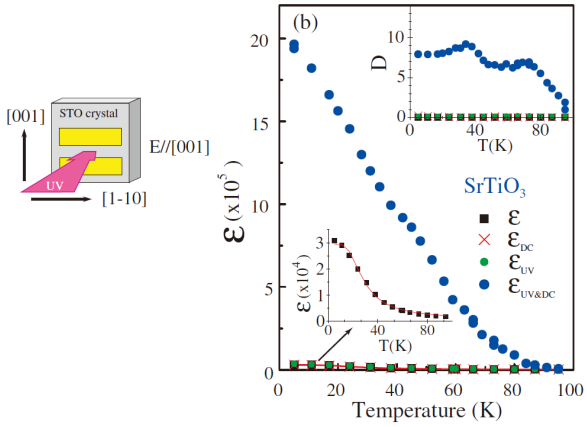

Figure 1-11: UV-induced drastic increase in the dielectric constant of quantum paraelectric $SrTiO_3$ under weak DC Electric Field [41]

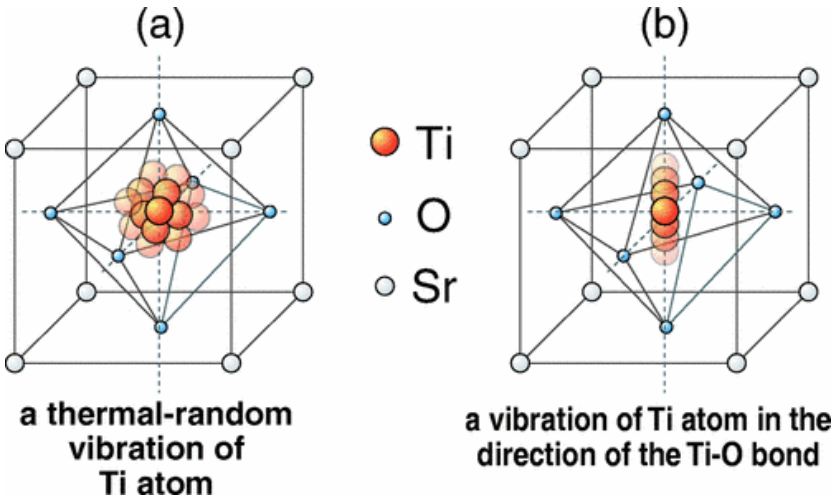

Figure 1-12: (a) Random vibration of Ti ions under thermal perturbation and (b) UV-induced vertical vibration of Ti ion in $SrTiO_3$ [15].

1.5 Objective of this study

Based on the response to UV irradiation, the changes in the physical property differ depending on the titanium–oxygen polyhedra. Because the titanates belonging to the fresnoite family with TiO_5 polyhedron exhibit excellent PL property under UV irradiation, they can be a good substitute for rare-earth-doped phosphors. However, the electronic in-gap states essential for realizing the PL property are unclear. XANES, which is corresponding to the electronic transition from the core level to the unoccupied electronic states, is a good approach to in-gap states. $SrTiO_3$ exhibits PL at low temperature as well with UV irradiation, which speculates a small distortion of TiO_6 octahedron in $SrTiO_3$. EXAFS, which is capable to measure the distance between atoms, is a suitable way to measure the distortion. Previous studies on the pre-edge of Ti K-edge XANES have proposed the enhancement of Ti ion vibration along the c-axis with UV irradiation. This physical phenomenon should be investigated by EXAFS.

In this thesis, the influence of the disorder of titanium–oxygen polyhedra is examined quantitatively, considering the UV effect. XAFS is adopted as the basic experimental approach. The objectives of this research are listed below:

(1) The electronic states of the titanate phosphors belonging to the fresnoite family are investigated via XANES to evaluate the role of TiO_5 polyhedron in the PL process. To reveal the energy diagram of the PL process, the origin of in-gap states must be clarified based on the experimental results and theoretical calculations.

(2) The local structure around the Ti atom in $SrTiO_3$ is investigated via EXAFS to detect the distortion of TiO_6 octahedron. Then, the origin of PL property in $SrTiO_3$ at low temperature is investigated.

The titanium–oxygen polyhedra and related physical properties were discussed in this section. The other four sections presented in this thesis are presented below. Sample preparation and XAFS experiment are discussed in the "Experiment" section. To overcome the different penetration of UV and X-ray, superfine powder was obtained by using a micron-sized sieve. The influence of UV was analyzed by irradiating UV light on the sample during the XAFS experiment. The electronic states of the self-activated titanate phosphors obtained by XANES are described in the third section. Then, the role of TiO_5 polyhedron in realizing the PL property is presented. In the fourth section, the origin of PL property in $SrTiO_3$ is studied by measuring the small distortion of TiO_6 octahedron. EXAFS is adopted as the main technique to detect this small distortion. In the "Conclusion" section, the relationship between the PL property of titanates and the TiO_5 polyhedron is summarized.

2 Experimental Techniques

2.1 Sample preparation

2.1.1 Self-activated titanate phosphor powder

The self-activatied titanate phosphor samples ($Ba_2TiSi_2O_8$, $Sr_2TiSi_2O_8$, and Na_2TiSiO_5) were synthesized via the conventional solid-state reaction method. Commercial $BaCO_3$, $SrCO_3$, Na_2CO_3, TiO_2, and SiO_2 powders with a purity of higher than 99% were used as raw materials. They were weighed and mixed to obtain uniform stoichiometric mixtures of three samples. To obtain homogeneous compositions, all the mixtures were carefully ground, and then pressed into pellets. The pellets of $Ba_2TiSi_2O_8$ and $Sr_2TiSi_2O_8$ were annealed at 1000°C for 12 h under air atmosphere, and were ground again. After repelletization, the pellets were calcined at 1300°C under air atmosphere for 2 h. The final powder samples were obtained by grinding the pellets. Na_2TiSiO_5 was prepared following the same procedure, with the exception of the annealing and calcination temperatures of 600°C and 850°C, respectively.

X-ray diffraction:

Because XAFS is very sensitive to the composition of measuring sample, the XRD patterns of these powder samples were recorded on an X-ray powder diffractometer with Cu K radiation (Rigaku, Miniflex) to check the purity and degree of crystallinity. A Rietveld refinement analysis was performed to confirm and analyze the XRD data.

Figure 2-1 compares the observed XRD patterns of $Ba_2TiSi_2O_8$, $Sr_2TiSi_2O_8$, and Na_2TiSiO_5 with the calculated patterns obtained from Rietveld refinement analysis, which demonstrates the high crystallinity of the samples. The intensities of the observed and calculated patterns were normalized to unity. The crystal parameters obtained from our Rietveld analysis are listed in Table 2-1, which are comparable to the previously reported values [25, 43, 44]. The corresponding crystal structures are illustrated in the insets in each panel of Figure 2-1, which highlight the TiO_5 polyhedra. The top two panels exhibit similar diffraction patterns because the crystal structures of $Ba_2TiSi_2O_8$ and $Sr_2TiSi_2O_8$ belong to the same fresnoite

structure with the tetragonal space group P4bm. A small amount of impurities exists in these two samples, as indicated by the arrows. However, neither SiO_2 nor $SrTiO_3$ affect the Ti K-edge XAS spectra because the signal is relatively weak. No impurity peak was observed for Na_2TiSiO_5. As shown in the XRD patterns in Figure 2-1, Na_2TiSiO_5 has another different crystal structure with the orthorhombic space group Pmc21. This structure contains TiO_5 polyhedral as well, as depicted in the inset.

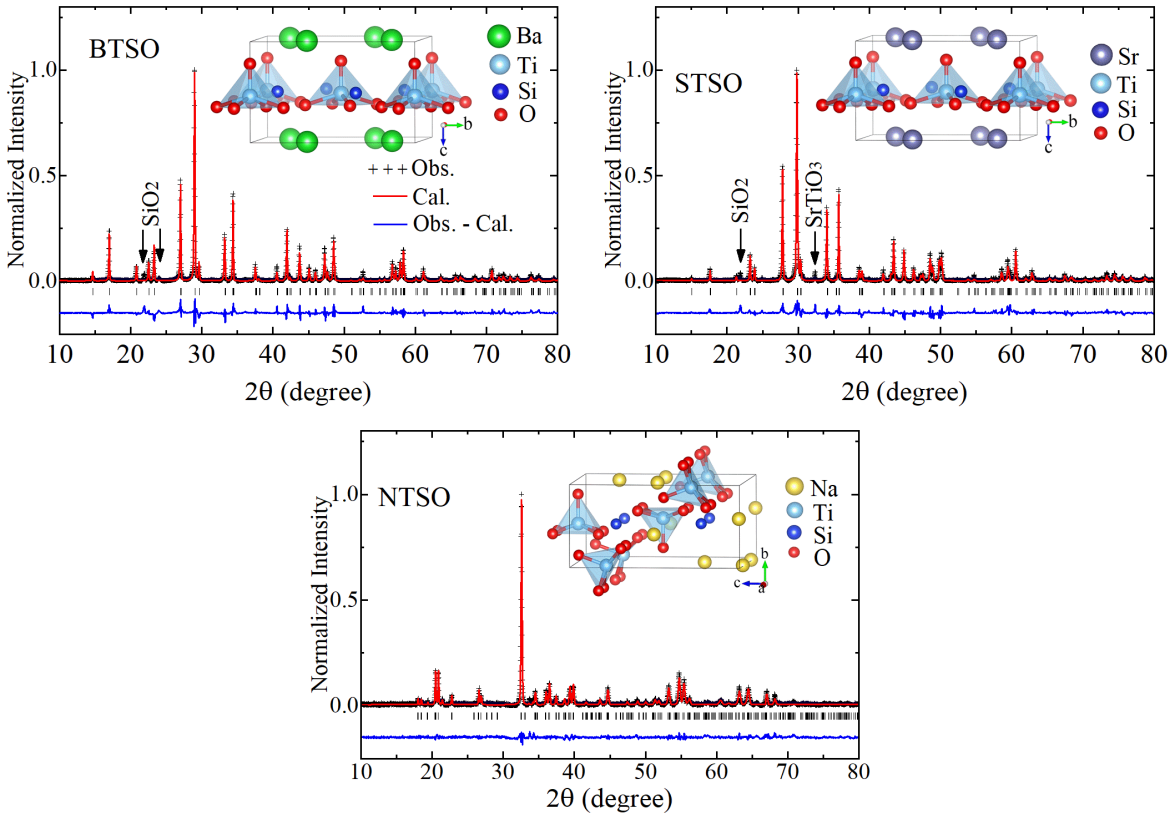

Figure 2-1: Rietveld refinement results for XRD patterns of $Ba_2TiSi_2O_8$, $Sr_2TiSi_2O_8$, and Na_2TiSiO_5. The experimental data are indicated by cross marks, and the calculated data are represented by red line. The difference between the observed and calculated patterns are shown in the lower part of each panel. Impurities are indicated by arrows. $Ba_2TiSi_2O_8$ and $Sr_2TiSi_2O_8$ show a similar crystal structure and contain the TiO_5 polyhedron, Na_2TiSiO_5 possesses a different crystal structure, but contains the TiO_5 polyhedron.

Table 2-1: Refined crystal parameters of $Ba_2TiSi_2O_8$, $Sr_2TiSi_2O_8$, and Na_2TiSiO_5

Sample	$Ba_2TiSi_2O_8$	$Sr_2TiSi_2O_8$	Na_2TiSiO_5
a(Å)	8.519(3)	8.323(5)	9.128(1)
b(Å)	8.519(3)	9.323(5)	4.801(4)
c(Å)	5.211(7)	5.024(7)	9.823(5)
$\alpha = \beta = \gamma$	90°	90°	90°
Space Group	Pb4m	Pb4m	$Pmc2_1$
χ^2	1.826	1.563	1.853

Fluorescence spectrophotometer:

The photoluminescence spectra were obtained using a fluorescence spectrophotometer with Xe lamp as the light source (Hitachi, F-2700). The bandpass of the spectrophotometer was set to 2.5 nm, thereby ensuring a high energy resolution (< 0.08 eV) for the entire spectrometer range. A 300 nm longpass filter was used to block the excitation beam.

Figure 2-2 shows the photoluminescence excitation (PLE) and PL spectra of the three samples. The monitored wavelengths of the PLE spectra were set to the peak wavelength of the corresponding PL spectra, and the excitation wavelengths of the PL spectra were set to the peak wavelengths of the corresponding PLE spectra. All the spectra were normalized to unity at their respective maxima. All the spectral profiles are similar; specifically, the PLE spectra of $Ba_2TiSi_2O_8$ and $Sr_2TiSi_2O_8$ overlap, because they are isomorphic to each other. However, the PL spectra of these two samples show a slight difference in their peak positions: 450 nm for $Ba_2TiSi_2O_8$ and 492 nm for $Sr_2TiSi_2O_8$. The energy difference is 0.23 eV, which can be discerned by the naked eye, as shown in Figure 2-2(e) and 2(f). $Ba_2TiSi_2O_8$ emits bright bluish-white light, whereas $Sr_2TiSi_2O_8$ emits yellowish light under UV irradiation. Furthermore, Na_2TiSiO_5 emits bluish-white light as well, similar to $Ba_2TiSi_2O_8$ (Figure 2-2(g)). Although the crystal structure of Na_2TiSiO_5 differs from that of the two other phosphors, as explained in the previous passage, the PL and PLE spectra of Na_2TiSiO_5

exhibit some similarities with those of $Ba_2TiSi_2O_8$ and $Sr_2TiSi_2O_8$. These similarities confirm that the TiO_5 polyhedra, which are contained in all three samples, play an important role in determining the PL properties of self-activated titanate phosphors.

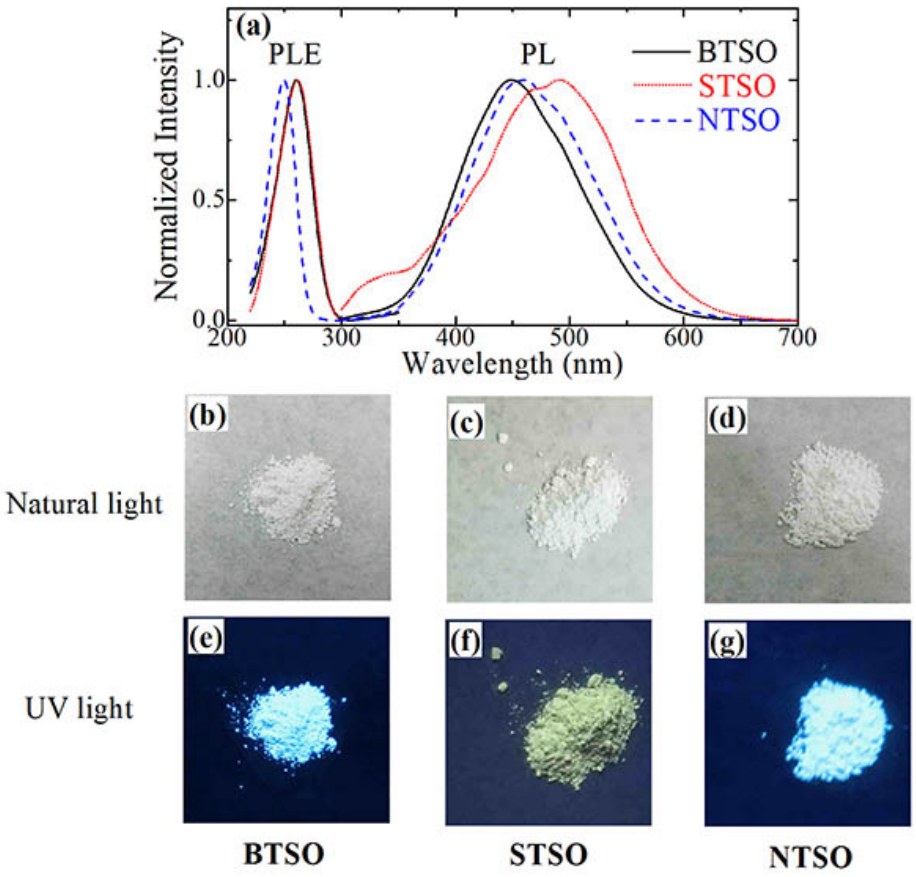

Figure 2-2: PL property of $Ba_2TiSi_2O_8$, $Sr_2TiSi_2O_8$, and Na_2TiSiO_5. (a) PLE and PL spectra of $Ba_2TiSi_2O_8$ (black line), $Sr_2TiSi_2O_8$ (red dot line), and Na_2TiSiO_5 (blue dash line). Images of $Ba_2TiSi_2O_8$, $Sr_2TiSi_2O_8$, and Na_2TiSiO_5 under (b–d) natural light and (e–g) UV light irradiation.

2.1.2 Fine strontium titanate powder

The raw material used for obtaining fine $SrTiO_3$ powder is an $SrTiO_3$ single crystal. First, the single crystal was ground by using a agate mortar. The obtained powder was transferred

Figure 2-3: 5 μm sieve was used for obtaining superfine $SrTiO_3$ powder. The net of this sieve is made of organic fiber and does not contain any metal.

to a beaker with ultrapure water to form a suspension of water and $SrTiO_3$ powder under ultrasonic treatment. Then, the suspended liquid was left still for 24 h, until the suspended liquid was separated into two layers. The bottom layer contained relatively larger $SrTiO_3$ particles and the top layer contained small particles.

To as-prepared superfine $SrTiO_3$ powder and the top layer liquid was flowed across sieves of 5 μm (Figure 2-3). The superfine $SrTiO_3$ powder was finally obtained after evaporating the water.

2.2 Synchrotron radiation

2.2.1 Basic information about synchrotron radiation

Synchrotron radiation is a type of electromagnetic radiation, and is emitted when relativistic charged particles move along curved trajectories when they are subject to a magnetic field [45]. A storage ring is used to produce electrons and maintain the electrons stored at constant energy and radio-frequency cavities. The advantage of synchrotron radiation is its wide spectral range, which covers infrared light to hard X-rays. Thus, synchrotron radiation is used in many applications, such as determining the material structures and properties in physics,

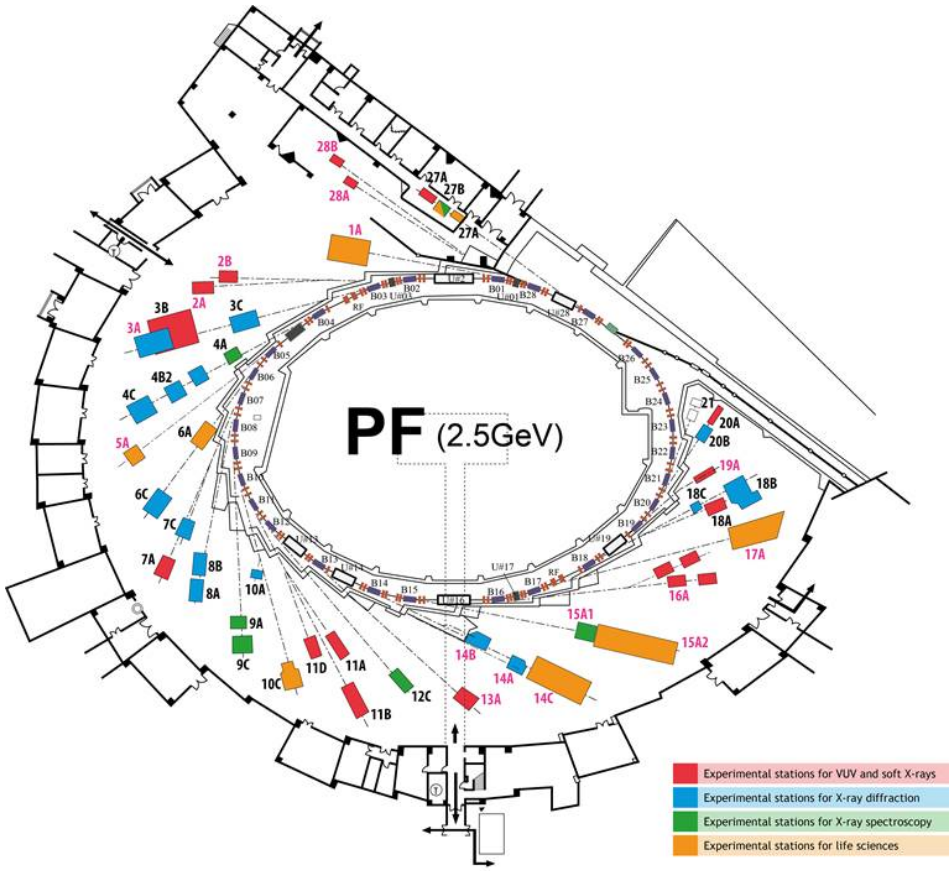

Figure 2-4: Layout of the Photon Factory storage ring and beamline distribution

chemistry, and biology, and even in disciplines such as archaeology and environmental science [46].

The main properties of synchrotron radiation are high intensity, polarization (both linear and circular), broad and continuous spectral range (from infrared light to hard X-ray region), natural narrow angular collimation, pulsed time structure, high brightness of the source due to the small cross-section of the electron beam and the high degree of collimation of the radiation, ultra-high vacuum environment, and high beam stability. All these properties can be quantitatively evaluated.

To date, three generations of synchrotron radiation sources have been developed, each with an improvement in quality. All the XAFS experiments in this research were conducted

at the Photon Factory (PF)(Figure 2-4), which is a second-generation synchrotron radiation.

2.2.2 Beamline 9A of Photon Factory

The experiments on Ti K-edge XANES of self-activated phosphors were conducted at the high-intensity, low-energy XAFS beamline BL-9A of the PF. The beamline layout of BL-9A is shown in Figure 2-5. An Si (111) double-crystal monochromator with water cooling was used for obtaining a wide photon energy range of 2.1–15 keV. Both transmission and fluorescent modes can be used in this beamline. The transmission mode can be used for powder samples, along with two ionization chambers for X-ray detection, whereas the fluorescent mode can be used for crystal samples or bulk samples; a 19-element silicon drift detector is used for avoiding self-absorption effects. To reduce high-order photons, a double flat mirror (Ni coated) is set in front of the sample set-up stage.

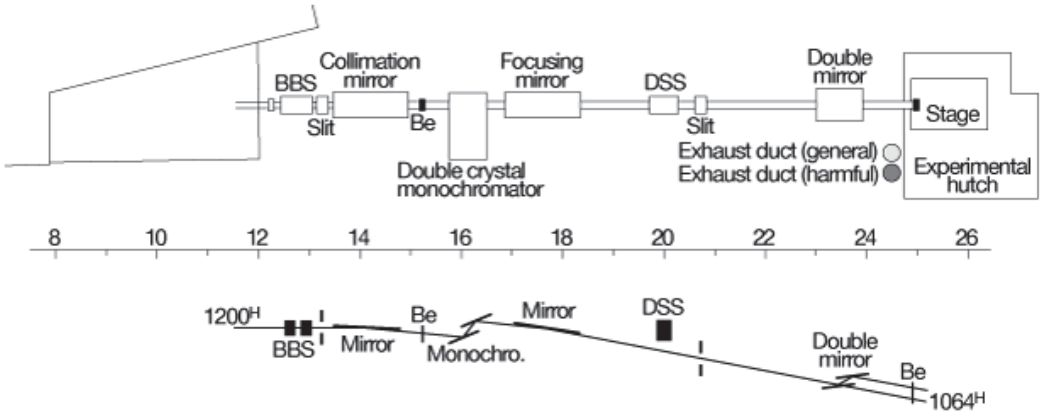

Figure 2-5: The beamline layout of BL-9A at the PF

2.2.3 Beamline 12C of Photon Factory

The experiments on Ti K-edge EXAFS of $SrTiO_3$ were conducted at the BL-12C: High throughput XAFS beamline BL-12C of the PF. The beamline layout of BL-12C is shown in Figure 2-6. An Si (111) double-crystal monochromator with water cooling was used for obtaining a wide photon energy range of 2.1–23 keV. Both transmission and fluorescent modes

Table 2-2: Beamline parameters of BL-9A at the PF

Energy range	2.1 - 15 keV
Measurement mode	Transmission and fluorescent
Magnetic field	Bending magnet
Monochromator	Si(111) Water-cooled double crystal
High order light reduction	Double flat mirror (Ni coated)
Energy resolution	$\Delta E/E \sim 2 \times 10^{-4}$ (9 keV)
Photon flux	6×10^{11} phs/s (7 keV)

can be used in this beamline. Compared with that of BL-9A, the energy range of BL-12C is significantly wider; therefore, XAFS for heavy element K-edge is available.

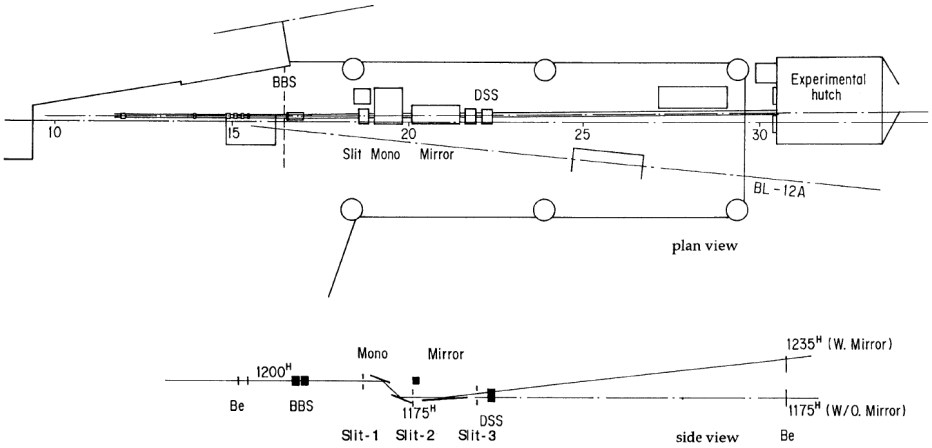

Figure 2-6: Beamline layout of BL-12C at the PF [47]

2.3 X-ray absorption

X-ray absorption is involved in the electron transition between two quantum states, namely, initial state and final state. Generally, the initial state is the core energy level, and is specific for each element, whereas the final state is located above the Fermi level. Because the final states can be modulated by the chemical and physical environments around

Table 2-3: Beamline parameters of BL-12C at the PF

Energy range	4 - 23 keV
Measurement mode	Transmission and fluorescent
Magnetic field	Bending magnet
Monochromator	Si(111) Water-cooled double crystal
High order light reduction	Double flat mirror (Ni coated)
Energy resolution	$\Delta E/E \sim 2 \times 10^{-4}$ (9 keV)
Photon flux	9×10^{11} phs/s (7 keV)

the absorbing atom, measuring the absorption coefficient of X-rays can provide reliable and useful information about the chemical and physical environments of the probe atom at the microscopic level. The electron transition is based on the Fermi's golden rule:

$$\mu \approx \sum |\left\langle \psi_{\mathrm{f}} | \mathrm{H}' \psi_{\mathrm{j}} | \right\rangle| \delta(\mathrm{E_f} - \mathrm{E_i} - \hbar\omega) \tag{2-1}$$

Generally, the absorption coefficient μ is a smooth function of energy:

$$\mu \approx \frac{\rho \mathrm{Z}^4}{\mathrm{ME}^3} \tag{2-2}$$

This equation shows that the absorption coefficient μ depends on the sample density ρ, atomic number Z, and atomic mass A. Because of this strong dependence of μ on both density ρ and atomic number Z, X-ray absorption is widely used in medical imaging, such as X-ray plate and X-ray computed tomography.

In an X-ray absorption experiment, we primarily measure the absorption coefficient μ, which produces the probability that X-rays will be absorbed according to the following equation (Beer-Lambert law), where $\mathrm{I_0}$ represents the X-ray intensity incident on a sample, t denotes the sample thickness, and I is the intensity transmitted through the sample. The relationship between these parameters is given by the Beer-Lambert law:

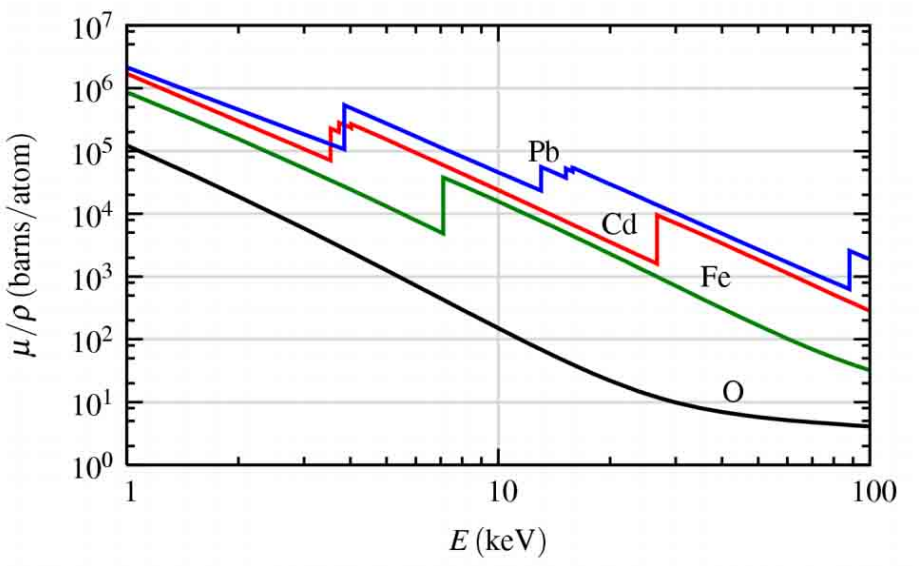

Figure 2-7: X-ray absorption spectra for several elements over the X-ray energy range of 1–100 keV. The spectra show strong energy dependence, and the sharp jumps in cross-section correspond to core-level binding energies of the atoms [48].

$$I = I_0 e^{-\mu t} \tag{2-3}$$

Generally, the absorption coefficient μ is a smooth function of energy. When the incident X-ray equals to the binding energy of a core-level electron for a specific atom, a sharp increase in the absorption coefficient occurs. Customarily, the rising curve is named an absorption edge, which corresponds to the core level to the continuum. Figure 2-7 shows several absorption edges for several specific atoms.

Two different modes can be used in an XAFS experiment, namely, transmission mode and fluorescence mode. In the transmission mode, the intensity of the incident and the transmitted X-ray beams are measured in an ionization chamber placed on both sides of the sample (Figure 2-8 (a)). The absorption coefficient of the transmission mode μ is expressed as:

$$\mu(E) = \mathrm{In}\frac{I_0}{I} \tag{2-4}$$

In the fluorescence mode, the incident X-ray beam is generally measured in the ionization chamber. Because of the existence of X-ray fluorescence or Auger electrons, a secondary emission resulting from the absorption of X-rays can be measured by a multiple SSD detector, as shown in figure 2-8 (b). The absorption coefficient of the fluorescence mode μ is expressed as:

$$\mu(\mathrm{E}) \propto \frac{\mathrm{I_f}}{\mathrm{I_0}} \tag{2-5}$$

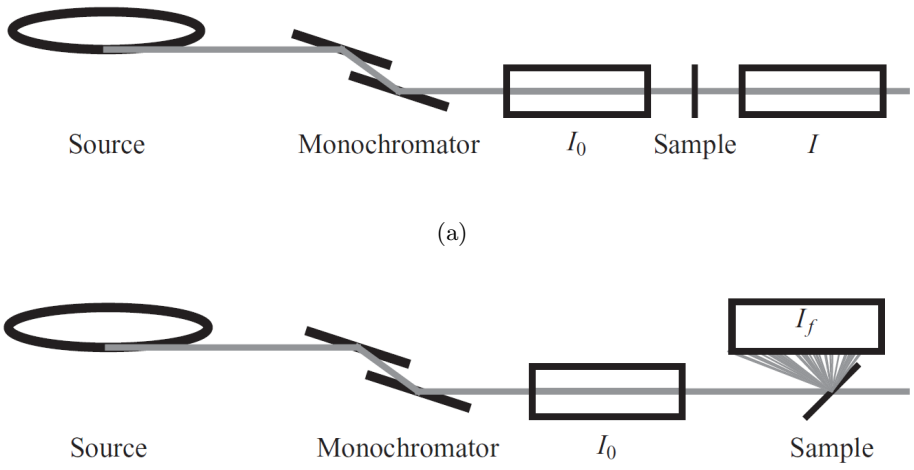

Figure 2-8: XAS experiment with (a) transmission mode and (b) fluorescence mode [9].

The equation of Fermi's golden rule indicates that XAFS is a modulation of X-ray absorption probability with the changing incident energy. Generally, the X-ray absorption spectrum is divided into two regimes: XANES and EXAFS. XANES is the X-ray absorption from the core level to the electronic states above the Fermi level. Because these electronic states are highly sensitive to formal oxidation states and the coordination chemistry of the absorbing atom, XANES is used to interpret the electronic information. EXAFS is the interference between the photoelectron wave and the scattering wave, which can be used to determine the distance, coordination number, and species of the neighbors of the absorbing atom. Figure 2-9 shows an Fe K-edge of XAFS [48].

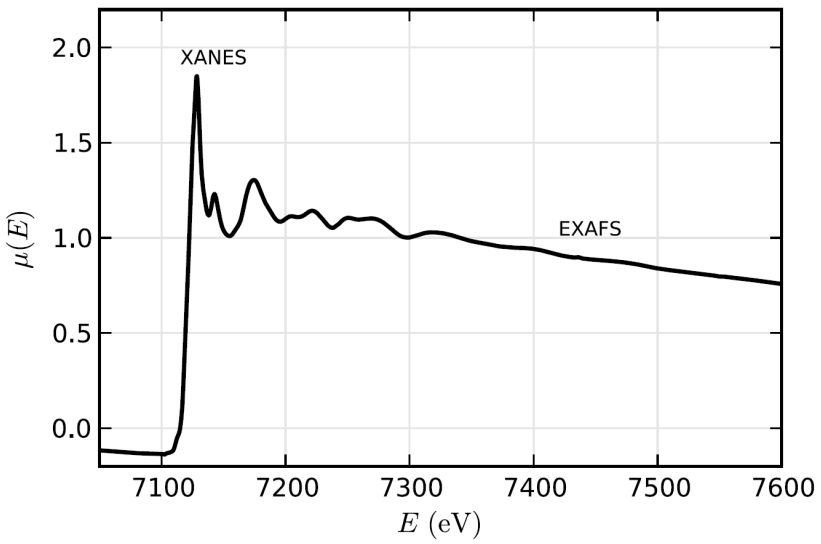

Figure 2-9: XAFS μ(E) for the Fe K-edge of FeO, showing the near-edge region (XANES) and the extended fine structure (EXAFS) [48].

2.3.1 X-ray absorption near edge structure

XANES is involved in the transition from the core level to the unoccupied states above the Fermi level (Figure 2-10). These unoccupied states are empty molecular orbitals, which correspond to the chemical bond states. The empty molecular orbitals are decided based on the local site symmetry and orbital occupancy. From the perspective of molecular orbital theory, the intensity and energy level of the pre-edge peaks correspond to the linear combinations of unoccupied empty molecular orbitals that have specific symmetry properties. Thus, the XANES spectrum can provide the symmetry information of the absorbing atom. In addition, because the possibilities of dipole transition and quadrupole transition differ greatly, XANES can identify the orbital types above the Fermi level as well.

Theoretical Calculation of XANES

Spectral simulations were performed for Ti K-edge XANES of the three samples using the finite difference method near edge spectroscopy (FDMNES) code [49]. In this code, a full potential calculation and relativistic corrections are employed for potential calculations with a self-consistent treatment, followed by the multiple scattering approach for XAS calculation.

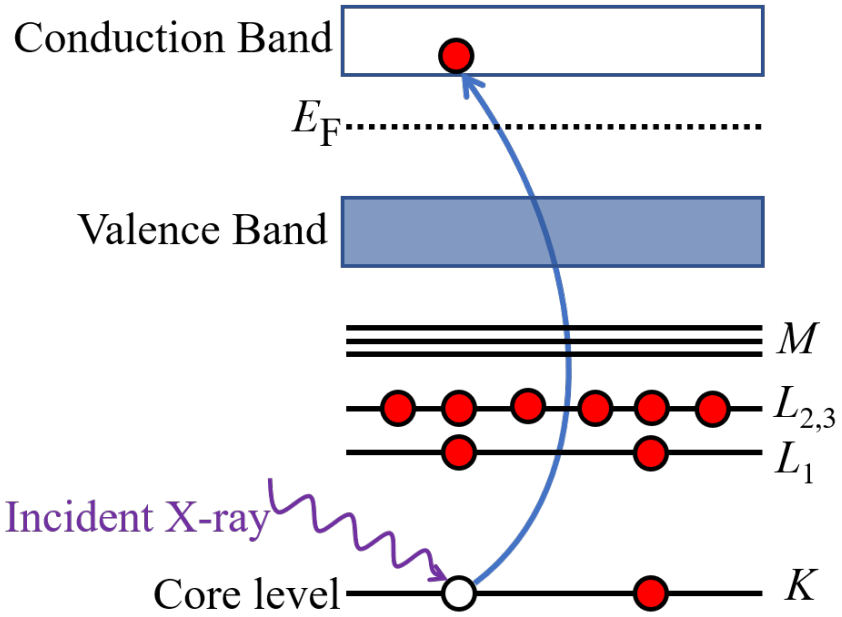

Figure 2-10: Schematic energy diagram of XANES. The electron in the core level was excited to the empty electronic states above the Fermi level, leaving behind a core hole

We assumed a cluster of radius 7.9 Å around a Ti ion using the crystal parameters obtained by XRD measurement. The local density of states (LDOS) of all constituent atoms were also calculated in the same runs.

2.3.2 Extended X-ray absorption fine structure

Because the incident X-ray energy is higher than the absorbing edge, the electrons will escape the atom; this is known as the photoelectric effect, and the emitted electrons are termed as photoelectrons because the absorbed X-ray is a photon. This process is illustrated in Figure 2-11.

The photoelectrons can be described as spherical waves propagating outward from the absorber atoms. These outgoing photoelectron waves can be scattered from the neighboring atoms (Figure 2-12). The interference of the outgoing waves and the scattered waves causes different features in the post edge, because the density of the unoccupied electron orbitals are

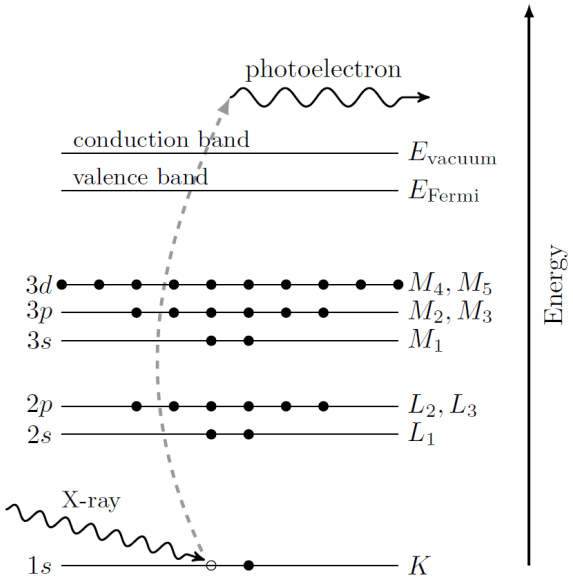

Figure 2-11: Photoelectric effect, in which the core-level electron was excited by X-rays having energy higher than the binding energy, leaving behind a hole in the core electron level. The photoelectron is promoted out of the atom [48].

modulated by the interference of the photoelectron waves [50].

Because the photoelectrons have the characteristics of waves, it is convenient to use the wavenumber to describe them. The converting equation from energy to wavenumber is given by 2-6.

$$\mathrm{k_{electron}} = \sqrt{\frac{2\mathrm{m}}{\hbar^2}(\mathrm{E_{photon}} - \mathrm{E_0})} \tag{2-6}$$

Because of the scattering process in the scattering atom, the phase of the scattered waves of a photoelectron is generally not the same as that of the outgoing wave. When the phase of the outgoing waves and scattered waves is the same at the absorber atom position, a crest in the post edge is produced, which corresponds to the maximum absorption coefficient (2-13). When the outgoing waves and scattered photoelectron waves are completely out of phase at the center of the absorber atom, a valley is produced, which corresponds to a decrease in the absorption coefficient.

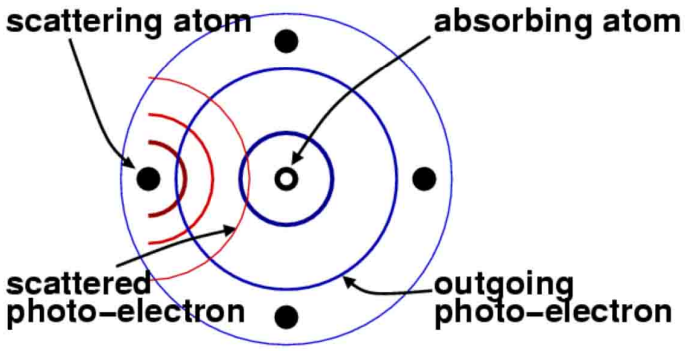

Figure 2-12: Interference of outgoing photoelectron waves from the absorbing atom and scattered photoelectron waves from the scattering atom.

The occurrence of "in phase" or "out of phase" is determined by the photoelectron wavelength and the interatomic distances between the absorber and the scattering atoms. The average distance between the absorber and the neighboring atoms does not change. According to the energy and wavenumber conversion equation, with the increasing incident X-ray energy, the wavelength of the photoelectron wave decreases progressively, and the interference of the two waves will be in phase and out of phase periodically. This causes an oscillation of the absorption coefficient in the post edge. Using these oscillations, the average distances between the absorber and the scattering atoms can be measured. In addition, as the energy of the incident X-ray is increased above the edge, the photoelectron wavelength decreases; therefore, increasing the energy range will improve the measurement accuracy.

EXAFS data analysis

To extract the EXAFS oscillation from the post edge, the data $\mu(E)$ must be processed by normalization and subtraction of the background. In this process, the pre-edge is fitted using the Victoreen formula, and then extrapolated to all energies in the measurement range of the data [8]. By subtracting the fitted Victoreen formula from μ(E), the pre-edge portion of the data was reduced to 0. The pre-edge subtracted data were then divided by the edge jump, following which the value of XAS in the post edge was normalized to 1. The conversion of $\mu(E)$ to the EXAFS oscillation $\chi(k)$ is based on the equation 2-7.

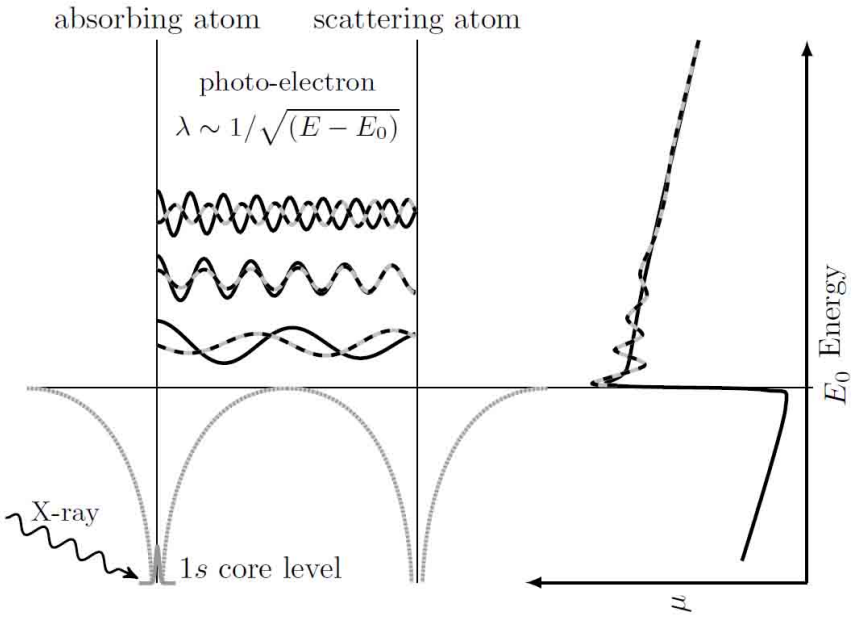

Figure 2-13: Schematic diagram of the modulation of the absorption coefficient of X-ray by the scattering photoelectron. The in-phase modulation between the outgoing photoelectron wave and the scattering photoelectron wave causes a crest in the EXAFS region, and the out-of-phase modulation causes a valley [48].

$$\chi(\mathrm{k}) = \frac{\mu(\mathrm{E}) - \mu_0(\mathrm{E})}{\Delta\mu_0} \tag{2-7}$$

In actuality, because of the complexity of the surrounding environment of the absorber, many factors must be considered to model the interference between the outgoing waves and the scattered waves . First, because the model of the spherical wave is used for describing the photoelectrons, a sinusoidal term is used; thus, the phase shift caused by scattering can be included in the sinusoidal term. Second, because each atom around the absorber can be a scatter, the sum of all the scattering paths is required to fit the experimental data. In addition, the amplitude of each path is infected by the scattering process and atom vibration. The theoretical EXAFS oscillation formula is expressed as follows:

$$\chi(\mathrm{k}) = \sum_{\mathrm{j}} \frac{\mathrm{N_j S_0^2(k) F_j(k)}}{\mathrm{kR_j^2}} \exp[-2\mathrm{k}^2\sigma_{\mathrm{j}}^2 + \frac{2}{3}\mathrm{C_{4j}k^4}]\mathrm{e}^{-2\mathrm{R_j}/\lambda_{\mathrm{j}}} \sin(2\mathrm{kR_j} + \psi_{\mathrm{j}}(\mathrm{k}) - \frac{4}{3}\mathrm{C_{3j}k^3}) \quad (2\text{-}8)$$

The meaning of each parameter is defined below [8]:

- Scattering amplitude $\mathrm{F}_j(\mathrm{k})$: proportionality constant, which is itself proportional to the possibility of scattering elastically off of the atom.
- j is the path number of each scattering path, including single scattering paths and multiple scattering paths. To modulate the absorption probability, the sum of all the scattering paths will be included, and each of these scattering events contributes separately, which results in a linear combination of each path.
- $\psi_j(k)$: phase shift caused by the local potential around the absorber and the scatterer.
- λ_j: mean free path of the photoelectrons, which causes the inelastic scattering and decay of the core hole.
- N is the coordination number or degeneracy. Around the absorber, several scattering atoms belong to the same species with an identical distance. To group them, degeneracy is used to be multiplied on a single path. For single scattering paths, N is referred to as the coordination number.
- $\mathrm{S_0^2}$ is the amplitude reduction factor. Once a photoelectron has been ejected from the atom, a core hole is created at the core level. The screening effect of the core level electrons reduces, causing all the other electrons to feel more positive charge from the nucleus, and the orbitals adjust to this change. Irrespective of the activity of the photoelectron, the final state of the absorbing atom is not the same as the initial state. The amplitude reduction factor is an element-dependent constant.
- σ^2 is defined by the variance in the half path length, i.e., the square of the standard deviation of the half path length $\left\langle (r - \overline{r})^2 \right\rangle$, always termed as the mean square relative displacement (MSRD) or Debye-Waller factor. It is used to correct for the difference between the experimentally determined and the theoretical $\chi(\mathrm{k})$ functions.

- R is the half path length. For single-scattering paths, the half path length is simply the average distance between the absorbing and scattering atoms. To compensate for the difference between the real value of half path length and the assumed value in the starting structure, δR is used.

- ΔE_0: Equation 2-6 describes the relationship between E_0 and wavenumber. E_0 is the energy used to calculate the momentum of the photoelectron. Because it is' difficult to obtain an exact value of E_0, ΔE_0 is used to adjust E_0.

- The higher-order cumulants C_3 and C_4 are the further correction of the EXAFS formula, which are defined by $\left\langle (r-\bar{r})^3 \right\rangle$ and $\left\langle (r-\bar{r})^4 \right\rangle - C_2^2$, respectively. C_3 and C_4 are not generally used in the EXAFS data analysis.

During the EXAFS data analysis, the scattering amplitude $F_j(k)$ $\psi_j(k)$: the phase shift λ_j: the mean free path of the photoelectrons is obtained from the assumed initial atom structure and the calculation procedure of the path data [51]. Based on the effect on χ, all the other parameters defined above can be categorized into two: (a) intensity-related parameters, namely, amplitude reduction factor S_0^2, Debye-Waller factor σ^2, C_4, path number j, and degeneracy N, which can affect the oscillation intensity of χ; (b) half path length R, ΔE_0, and C_3, which can affect the phase of χ.

Because the parameters in each group are highly correlated, it is difficult to obtain a reasonable value for several parameters simultaneously. Thus, the common approach is to fix one of them and guess the other. For example, the amplitude reduction factor S_0^2 and Debye-Waller factor σ^2 are highly correlated and affect the intensity of χ. Therefore, to find a reasonable physical value of σ^2, S_0^2 must be fixed with a specific value. The same approach is equally applicable for the phase-related parameters as well.

Equation 2-8 describes the EXAFS oscillation caused by the interference of the outgoing and the scattering photoelectron waves. To obtain the atomic distance, Fourier transform must be used:

$$\chi(R) = FT(\chi(k)) = \frac{1}{\sqrt{2\pi}} \int_0^\infty k^n \chi(k) W(k) e^{i2kR} dk \tag{2-9}$$

As mentioned above, the wider range of X-ray energy measurement can improve the accuracy

of the experimental measurement. However, with the increasing energy, the wavenumber becomes longer, the amplitude of EXAFS oscillation delay fast. To emphasize the oscillations at large wavenumbers, χ(k) is multiplied by a power of k, as shown in the Fourier transform equation above.

To perform an EXAFS data analysis from the raw data to the reasonable value of each parameter, several software packages are required. The scattering paths are calculated by FEFF [51], which is an ab initio multiple-scattering code for calculating the excitation spectra and electronic structure. The background reduction process of experimental data can be accomplished using the software Athena. The fitting procedure of the experimental raw data and theoretical calculations can be performed using Artemis or FEFFIT. Artemis is contained in the Demeter package and IFEFFIT package along with Athena [52, 53]. FEFFIT has the same algorithm as Artemis. In this study, FEFFIT is used in the fitting procedure [54].

3 Investigation of the electronic states of TiO_5 polyhedron containing self-activated titanate phosphors by XANES

3.1 Experimental setup and configuration

The XANES experiments were performed in the beamline 9A of the PF. The spectra were measured in the transmission mode at 100 K. The powder samples were spread over adhesive tapes at a sufficiently low thickness to accommodate the effective penetration depths of UV and X-ray radiation. The tape was then fixed on a rectangular copper sample holder (Figure 3-1 a). Two factors were considered in the designing of experiments: temperature control and UV irradiation. The temperature was controlled by a closed-cycle helium cryostat. The sample holder was placed at the center of the chamber of the cryostat. To allow UV light irradiation on the chamber, one side of the Kapton film window was replaced with SiO_2 glass (Figure 3-1 b).

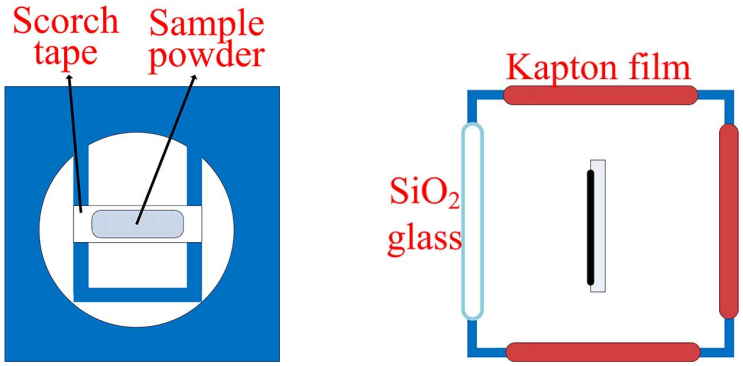

(a) (b)

Figure 3-1: Schematic of the sample setup. (a) Spreading of powder over the Scorch tape, and (b) vertical view of the cryostat chamber.

To ensure that the sample is irradiated by X-ray and UV light simultaneously, an angle of 45° was set between the direction of the X-ray and the plane of the sample holder (Figure 3-2 (a)). The sample powder on the Scorch tape was faced toward the SiO_2 glass window (Figure 3-2 (b)).

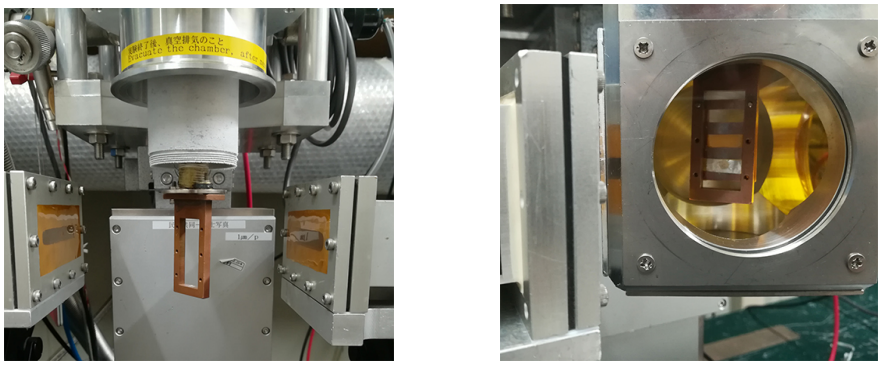

(a) (b)

Figure 3-2: (a) Sample holder makes an angle of 45° to the incoming direction of X-rays, (b) the sample within the direction where light is allowed to irradiate the sample through an SiO_2 glass window.

An Hg-Xe lamp (Lightningcure LC8, Hamamatsu, Japan) was used as the UV light source. The UV light was guided by an optical fiber onto the sample, and the UV power on the sample was controlled by a neutral density filter from 0 to 500 mW cm^{-2}. Because the excitation energy of self-activated phosphors is approximately 250 nm, a 250 nm band-enhanced type lamp was selected. To ensure the irradiation of sufficient intensity of UV light on the sample, a condenser lens was placed in front of the optical fiber.

Figure 3-3: Hg-Xe lamp used as the UV light source in our experiments. The condenser lens were used in the tail of the optical fiber to focus the UV light.

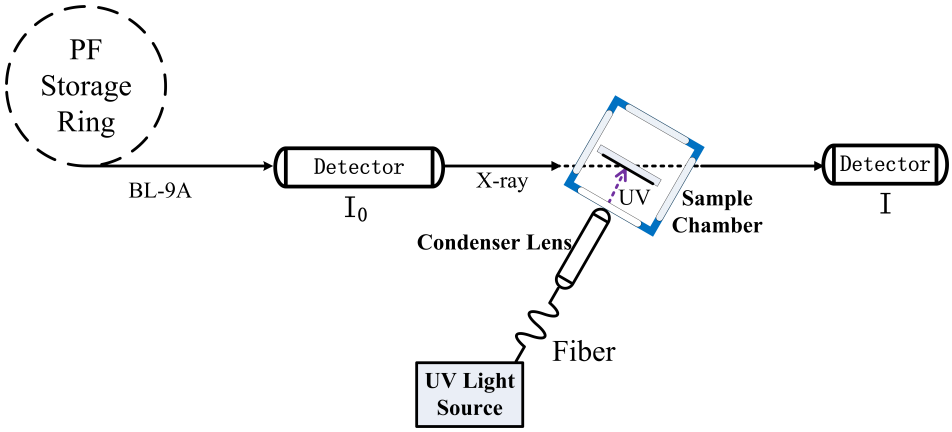

Figure 3-4: Schematic of the XAFS experiment in BL 9A with UV irradiation.

The experiments on Ti K-edge XANES of self-activated phosphors were performed at the beamline BL-9A of the PF at the Institute of Materials Structure Science. A schematic illustrating the XAFS experiment with UV irradiation is shown in Figure 3-4. The angular position of the monochromator crystals was calibrated using the Ti K-edge threshold at 4985.3 eV of standard $BaTiO_3$ powder. The X-ray energy was varied using an Si (111) double monochromator, and higher-order harmonics were removed using a double flat Ni-coated mirror. The overall energy resolution of the beamline was 0.1 eV. For each sample, the XANES spectra with and without UV irradiation were measured. The UV irradiation on the powder was controlled at 162 mW, 324 mW, and 487 mW.

3.2 Ti K pre-edge XANES of titanate compounds

Figure 3-5 shows the Ti K-edge XANES of Ba_2TiO_4, $Ba_2TiSi_2O_8$, and $SrTiO_3$. $SrTiO_3$ contains TiO_6 octahedron with O_h symmetry. As shown in section 1.2, the $3d$ orbitals will be split into t_{2g} and e_g energy levels. The first two peaks of Ti K pre-edge of $SrTiO_3$ are corresponding to the t_{2g} and e_g electronic states. $Ba_2TiSi_2O_8$ contains TiO_5 square pyramid polyhedron with C_{4v} symmetry. The intensity of the pre-edge of the TiO_5-containing materials is significantly higher than that of the TiO_6-containing materials. This can be explained by the symmetry reduction. The symmetry reduction from O_h to C_{4v} is generally regarded to be caused by Ti ion displacement in a TiO_6 polyhedron along the vertical direction. In the

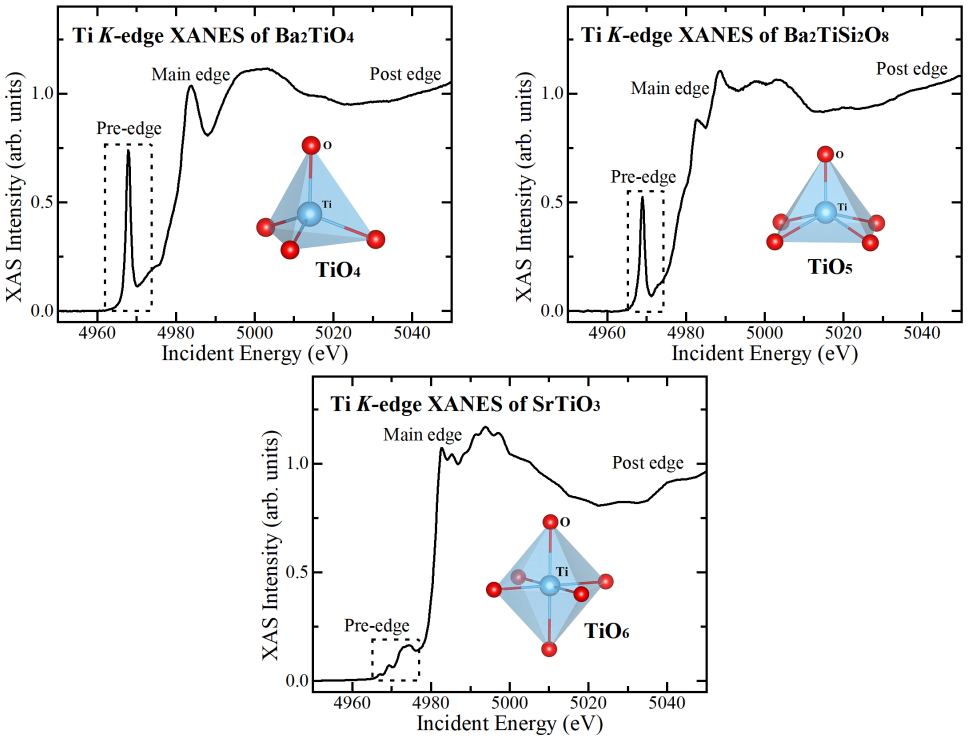

Figure 3-5: Ti K-edge XANES of Ba_2TiO_4, $Ba_2TiSi_2O_8$, and $SrTiO_3$. The structure of titanium–oxygen polyhedra (TiO_4, TiO_5, and TiO_6) contained in each material are inserted in each figure, respectively. The pre-edge features are noted by the dotted rectangle.

C_{4v} symmetry, the $3d_{3z^2-r^2}$ orbital can hybridize with $4p_z$ orbital, which is parity forbidden in the O_h symmetry. This hybridization makes the electronic transition dipole allowed and results in high pre-edge peaks. It's worth noting that the second pre-edge peak in the TiO_6 octahedron and the giant pre-edge peak in the TiO_5 polyhedron have the same e_g origin, so the intensity of the pre-edge of the TiO_5 polyhedron is interpreted based on the magnitude of Ti displacement [55]. In the case of Ti K pre-edge of XAS of Ba_2TiO_4, not only the intensity of the pre-edge is much more higher than that of the other two polyhedra, the energy level also varies slightly toward lower energy. The Ba_2TiO_4 contains TiO_4 tetrahedron with T_d symmetry. In the T_d symmetry, the 5-degenerate $3d$ orbitals and 3-degenerate $4p$ orbitals are highly hybridized to form equivalent orbitals. These orbitals are used to bond with the 4 oxygen coordination. The hybridization results in the high electronic transition and energy level shifting.

3.3 Ti K pre-edge XANES of self-activated titanate phosphors

The Ti K-edge XAS spectra of the three samples are shown in Figure 3-6. All the spectra were normalized to unity at the peak maxima after the linear pre-edge backgrounds were subtracted. The overall spectral profiles are generally similar. The main edges above 4982 eV correspond to $1s$–$4p$ dipole transitions. Above the edges, the intensity ratio of the first two peaks, labeled as A and B, are identical in $Ba_2TiSi_2O_8$ and $Sr_2TiSi_2O_8$ because these two compounds are isomorphic; the sharp cusp (labeled A) is a characteristic of Na_2TiSiO_5. These minor differences above the edges reflect a slight difference in the Ti $4p$ states; however, the energy levels of the corresponding states substantially exceed (ca 15 eV) the Fermi level and are not related to the PL properties.

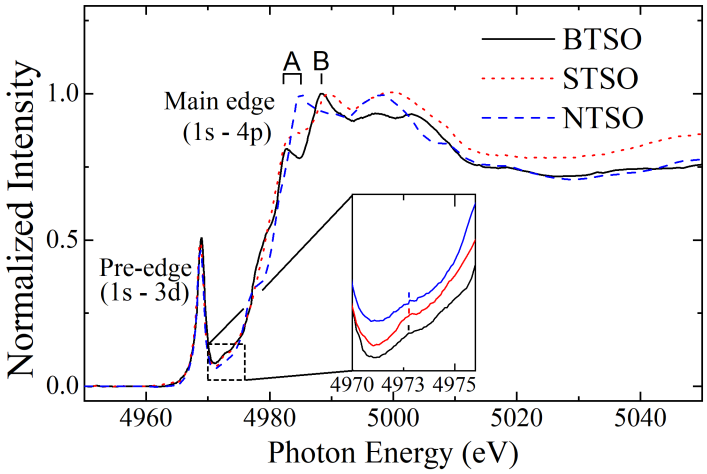

Figure 3-6: Ti K-edge XANES of $Ba_2TiSi_2O_8$ (black solid line), $Sr_2TiSi_2O_8$ (red dotted line), and Na_2TiSiO_5 (blue dashed line). The inset shows an enlarged view of the humps with offsets; humps are indicated by the vertical line.

Another characteristic of these spectra is a distinct peak at 4968.5 eV in the pre-edge region. Farges et al. reported that this peak can be attributed to the $1s$–$3d$ 'dipole' transition [56]. In general, the $1s$–$3d$ transition is dipole-forbidden, but quadrupole-allowed; therefore, the spectral intensity of the pre-edge features is weak compared with that of the main edge. For example, the pre-edge peak intensities of titanates with TiO_6 octahedra, e.g., SrTiO3 [57, 58], are less than one-tenth of that of the main edges. Through symmetry reduction, Ti

$3d$ orbitals start to hybridize with O $2p$ orbitals, following which the $1s$–$3d$ transition becomes dipole-allowed. The present three samples contain pyramidal TiO_5 polyhedra with a short Ti–O bond, which supports hybridization between the O $2p$ and Ti $3d$ orbitals. In addition, the isolation of TiO_5 polyhedra in the unit cell plays an important role in the creation of a distinct pre-edge peak. Farges et al. noted that the Ti $3d$ orbitals form molecular orbitals with O $2p$ orbitals in each isolated polyhedron, resulting in "bound states." This process leads to the creation of quasilocalized states just above the Fermi level.

Before discussing the UV irradiation effects, we consider the small humps observed between the pre-edge peaks and the main edges in all three samples. This region is enlarged in the inset of Figure 3-6. Because the hump is located above the pre-edge peak, it may serve as a trap for UV-excited electrons.

3.4 UV effect for Ti K pre-edge XANES of self-activated titanate phosphors

Because the characteristic high intensity for the giant pre-edge peak, the UV effect were firstly investigated. Figure 3-7 (a) shows the variation of the pre-edges of $Ba_2TiSi_2O_8$ with increasing the UV irradiation power. It is clear that the intensity of pre-edge peaks are decreased as UV power increasing. This phenomenon can be explained by the occupancy of the electronic states of the pre-edge by the UV excited electrons (figure 3-7 (b)). During the X-ray absorption, the occupancy of electronic states of UV excited electrons reduces the volume of electronic states for the X-ray excited electrons and therefore suppress the X-ray absorption. However, the UV energy is around 5 eV, so the electronic states for receiving the UV excited electrons should at the higher energy level than the giant pre-edge. The direct electron transition from the O $2p$ valence band to the in-gap pre-edge state is unlikely to occur. It may be assumed that the decrease of the pre-edge peak is caused by the de-excitation process of the UV-excited electrons mediated by the trap state. To find the electronic states of directly receiving UV excited electrons, the investigation for the electronic states at the higher energy level is required.

The UV effect on the hump of $Ba_2TiSi_2O_8$ is shown in figure 3-8 (a). The hump is enlarged

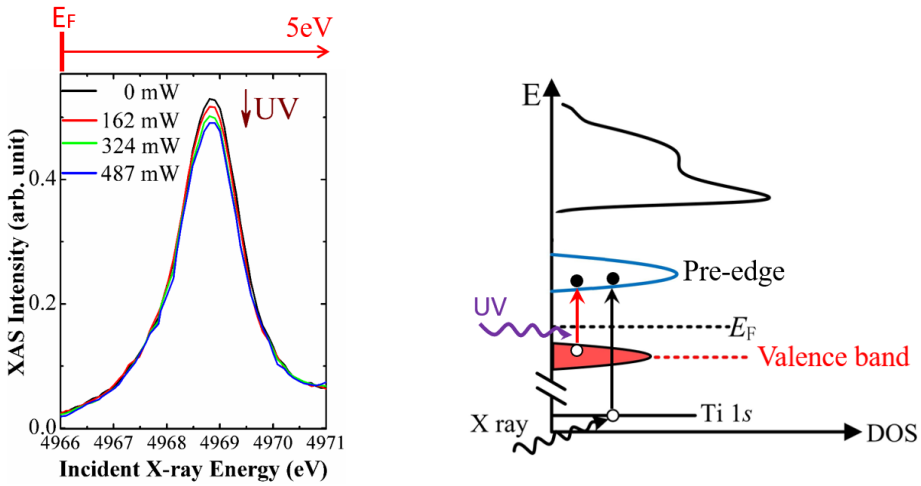

(a) (b)

Figure 3-7: UV effect for the intensity of the pre-edge of $Ba_2TiSi_2O_8$ (a). Schematic energy diagram of the occupancy of electronic states of pre-edge by the X-ray and UV excited electrons (b).

and underlined for indicating the variation of the intensity. It shows the intensity of hump are also decreased with increasing the UV irradiation power. This phenomenon can also be explained by the occupancy of the electronic states of the pre-edge by the UV excited electrons (figure 3-8 (b)). However, the amplitude of the decreasing intensity for hump is much more than that of the giant pre-edge, the hump is almost diminishing under the high UV irradiation power. This gives the proof that the electronic states of hump is directly occupied by the UV excited electrons. During the photoluminescence process, the electrons in the valence band was excited to the electronic states of hump by UV irradiation. The electron moves to the electronic states of pre-edge by the relaxation process. The electronic states of pre-edge act as in-gap states for producing the visible light emission. So the electronic states of hump act as electron traps for receiving the UV excited electrons. Therefore, the TiO_5 polyhedron is the the color center of the self-activated titanate phosphors, all the electronic states created by the TiO_5 polyhedron dominate the photoluminescence process.

For comparison, the UV effects observed in the XAS spectra of all three samples $Ba_2TiSi_2O_8$, $Sr_2TiSi_2O_8$ and Na_2TiSiO_5 are illustrated in Figure 3-9: the top three panels present the

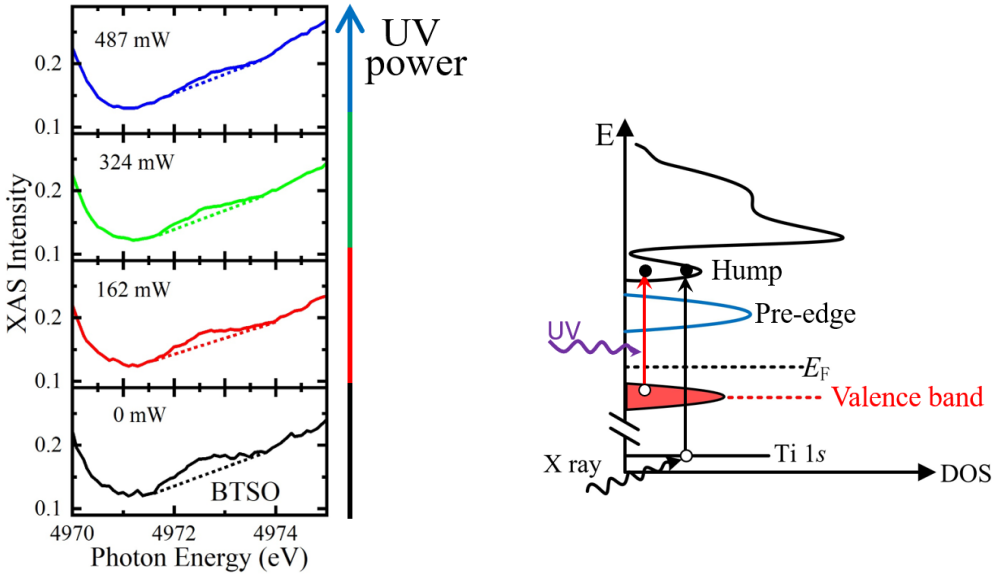

(a) (b)

Figure 3-8: UV effect for the intensity of the hump of $Ba_2TiSi_2O_8$ (a). Schematic energy diagram of the occupancy of electronic states of hump by the X-ray and UV excited electrons (b).

results for the pre-edge peaks, and the bottom three panels display the results for the humps. For all three samples, the intensity of the pre-edge peaks decreases slightly with the increasing UV irradiation; additionally, the hump intensity decreases with the same trend. This indicates the same mechanism of photoluminescence for all the three sample. In addiation, The electronic states of pre-edge act as in-gap states during the PL process. In addition, relative smaller intensity of hump in Na_2TiSiO_5 indicates the relative smaller electronic density of electron traps, which maybe explain the relatively lower emission than that of $Ba_2TiSi_2O_8$.

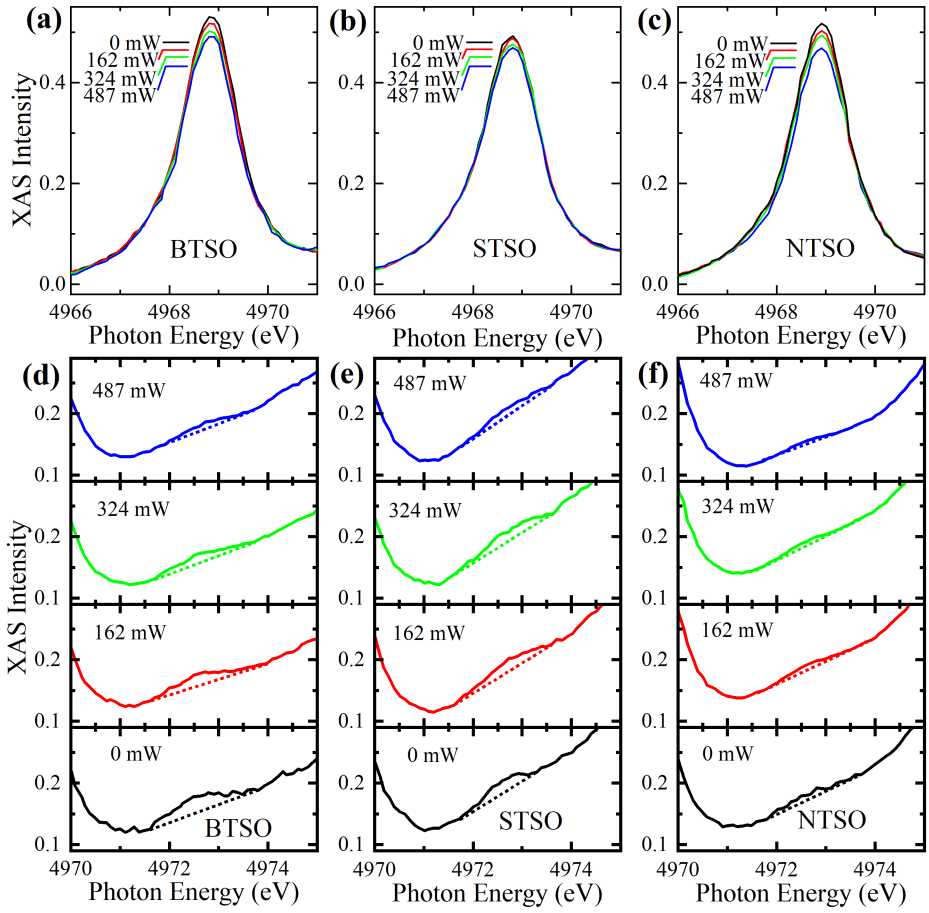

Figure 3-9: (a–c) show the UV effect for the intensity of Ti K pre-edge peaks for $Ba_2TiSi_2O_8$, $Sr_2TiSi_2O_8$, and Na_2TiSiO_5, respectively. The data of different UV output powders are indicated by lines of different colors. (d–f) show the UV effect for the intensity of hump for $Ba_2TiSi_2O_8$, $Sr_2TiSi_2O_8$, and Na_2TiSiO_5, respectively.

3.5 Theoretical calculation of Ti K pre-edge XANES of self-activated titanate phosphors

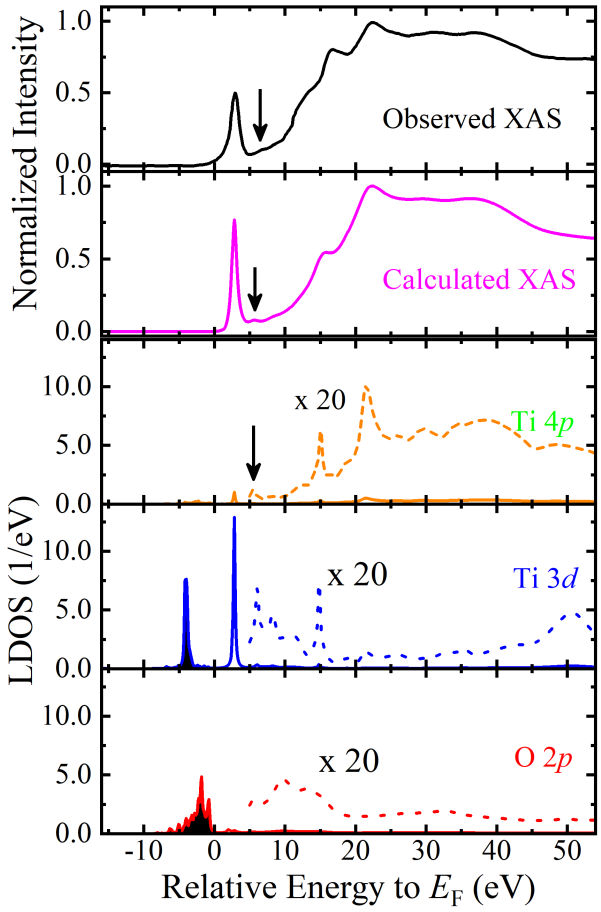

Figure 3-10: Theoretical calculation of Ti K-edge XANES of $Ba_2TiSi_2O_8$. The observed and calculated data are compared in the first two panels. The LDOS of Ti 3d, Ti 4p, and O 2p states are shown in the bottom three panels, respectively. The hump and its corresponding LDOS state are indicated by arrows.

To confirm the energy diagram proposed in the previous section, we calculated the Ti K-edge XAS results for the three samples using the FDMNES code. As an example, a calculated $Ba_2TiSi_2O_8$ spectrum is compared with the observed spectrum in Figure 3-10, together with the LDOS of the related orbitals. The shaded LDOS represents the occupied valence bands. The characteristic features are well-reproduced by the calculations. The

general spectral profile is similar to that of the Ti $4p$ LDOS, which can be simply understood as the Ti $1s$–$4p$ dipole transition. Notably, the pre-edge peak consists of both Ti $4p$ and Ti $3d$ states. The $3d$ LDOS is 10 times larger than the $4p$ LDOS, and is highly localized in the pre-edge region. In general, the $3d$ and $4p$ states are less-hybridized in the centrosymmetric coordination environment. By reducing the symmetry, i.e., TiO_6 to TiO_5, the centrosymmetry is broke with point group reducing from O_h to C_{4v}, the $3d$ and $4p$ belong to the same irreducible representation A_1 in the character table of C_{4v}. Therefore, the $3d$ and $4p$ states of an identical Ti ion start to hybridize with each other [59, 60]. This simulation results are consistent with the discussion in section 3.2. Thus, it can be concluded that the large pre-edge primarily originates from the intra-atomic hybridization between the Ti $3d$ and $4p$ states. The contribution of O $2p$ is less pronounced in this region, which is consistent with a previous study by Farges et al., in which destructive interference from nearest-neighbor oxygen atoms was reported [56]. The lower degree of hybridization is beneficial for PL because the UV-excited electrons from the O $2p$ valence band can survive longer in the unoccupied conduction band. The small hump is also reproduced in the calculated spectrum, as indicated by arrows, together with a corresponding component in the Ti $4p$ LDOS. Thus, the hump can be assigned to the Ti $4p$ sub-band.

After the in-gap states are determined by the XAS experiment and the origin of the in-gap states are illustrated by the theoretical calculation. The reason that $Sr_2TiSi_2O_8$ possesses different emission color with UV irradiation comparing to $Ba_2TiSi_2O_8$ and Na_2TiSiO_5 can be explained. The normalized pre-edge peaks of the three samples are compared in Figure 3-11. The peak position of $Sr_2TiSi_2O_8$ shifts toward lower energy by 0.2 eV compared with those of $Ba_2TiSi_2O_8$ and Na_2TiSiO_5, which corresponds to the red shift observed in the PL spectrum of $Sr_2TiSi_2O_8$ (Figure 2-2(a)). On this basis, it may be speculated that the electronic states of these pre-edge peaks are evidence of the color centers in these self-activated titanate phosphors.

The different energy position of the pre-edge peaks for $Sr_2TiSi_2O_8$ and $Ba_2TiSi_2O_8$ can be explained by the $3d$ orbitals splitting based on the crystal field theory. The energy level of $3d$ orbitals with octahedral and square pyramidal structure are shown in figure 3-12. As we have

showed above, $3d$ orbitals will be split into e_g and t_{2g} energy levels with O_h symmetry. When the symmetry is reduced to the D_{4h} point group with the lengthening the distance between the Ti ion and two apical O ions in the same extent or the shrinking the the distance between the Ti ion and four equatorial O ions in the same extent, the e_g and t_{2g} energy levels will be further split. Based on the crystal field theory, the potential strength between the ions is decided by the distance of the ions. Therefore, with the symmetry reduction from O_h to D_{4h}, the energy level of horizontal orbitals ($d_{x^2-y^2}$ and d_{xy}) will increase, the The energy level of vertical orbitals (d_{xz}, d_{yz}, and d_{z^2}) will decrease. The point group will further reduced to C_{4v} with the Ti ion displacement along the vertical direction. If the amplitude of this displacement is big, the bond between the Ti ion and the bottom O will be broken, which results the formation of the TiO_5 square polyhedron. The Ti ion displacement cause the shrinking distance between the Ti ion and the top O (noted by d in figure 3-12). The effect is that the energy level of horizontal orbitals ($d_{x^2-y^2}$ and d_{xy}) will decrease, the The energy level of vertical orbitals (d_{xz}, d_{yz}, and d_{z^2}) will increase. Especially, the d_{z^2} orbital has the whole vertical direction character, its energy level is easily influenced with the changing of the value d in the TiO_5 polyhedron. The value of d for $Ba_2TiSi_2O_8$ is 1.67 Å, smaller than the value 1.75 Å in $Sr_2TiSi_2O_8$. The electronic states of Ti K pre-edge in TiO_5-containing materials mainly originate from d_{z^2} orbitals. So the difference of energy position for pre-edge peaks of $Ba_2TiSi_2O_8$ and $Sr_2TiSi_2O_8$ stems from the different bond length d. This result points out a new way to characterize the Ti ion off-center displacement. In addition, the decreasing d also increases the orbital hybridization Ti $3d$ with Ti $4p$ and O $2p$. This is also the origin of the existence of the giant pre-edge peak in TiO_5-containing materials.

3.6 Energy diagram of self-activated phosphors

Based on the observed and calculated XAS spectra, a schematic energy diagram of PL and the Ti K-edge X-ray absorption process are illustrated in Figure 3-13. First, an incident X-ray excites a Ti $1s$ core electron to the unoccupied $4p$ state through dipole transition. A small amount of core electrons is transferred to the Ti $3d$ states through quadrupole transition, which is enhanced by the intense $3d$ LDOS to form a large pre-edge peak. Under UV irradiation, the

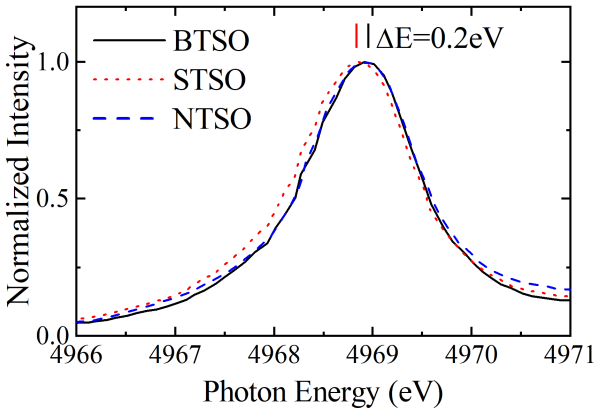

Figure 3-11: Normalized Ti K pre-edge peaks of $Ba_2TiSi_2O_8$ (black solid line), $Sr_2TiSi_2O_8$ (red dotted line), and Na_2TiSiO_5 (blue dashed line). The energy difference between the pre-edge peaks is represented by ΔE.

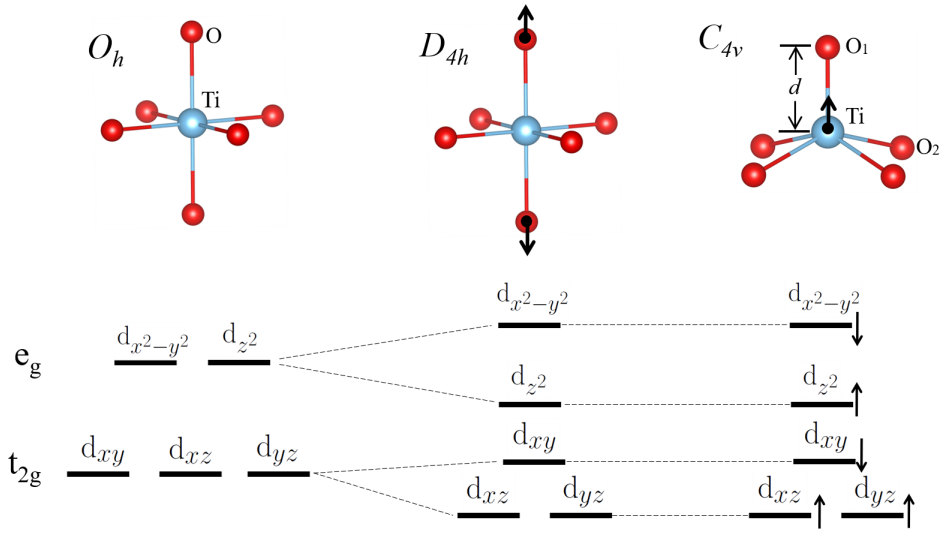

Figure 3-12: The 3d orbitals splitting with the symmetry reduction from O_h, D_{4h} to C_{4v}.

valence electrons are excited to the Ti 4*p* sub-band, followed by non-radiative relaxation to the lower Ti 3*d* state. The difference in the UV power dependence of the hump and the pre-edge peak is attributed to the different orbital characteristics of the relevant states. The hump originates from the Ti 4*p* orbital, whereas the pre-edge peak arises from the Ti 3*d* orbital. The intra-atomic 4*p*–3*d* hybridization should be beneficial for PL because it suppresses the direct recombination of UV-excited electrons with valence holes.

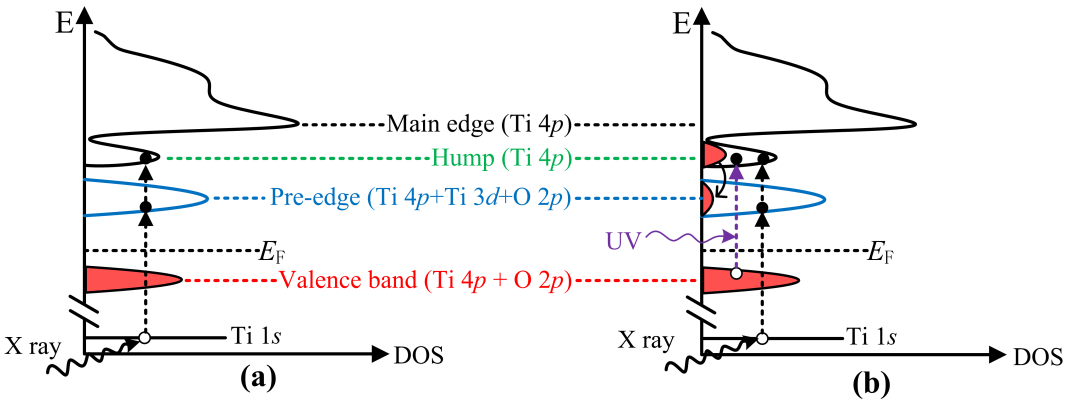

Figure 3-13: Energy diagram for self-activated titanate phosphors. (a) Schematic of X-ray absorption, (b) X-ray absorption and PL procedure. The competition for occupying the electronic states above the Fermi level between X-rays and UV light is indicated by the region in red.

3.7 Conclusion

The mechanism of photoluminescent procedure of self-activated titanate phosphors was investigated by Ti *K* pre-edge XANES. Two features were observed in the pre-edge region: a large pre-edge peak and a small hump. The influence of UV on these features was studied by irradiating UV light during the XANES experiment. The intensities of the large pre-edge peak and hump decreased with UV irradiation. From the perspective of electronic states, the decrease in the intensity of these features can be explained by the electron occupation of the corresponding electronic states with UV excitation, which explains the participation of these electronic states in the PL process. The relevant electronic states of these features were assigned using theoretical calculations based on the FDMNES code. The large pre-edge

peaks and humps arise from the intra-atomic Ti $3d$–$4p$ hybridization and Ti $4p$ sub-band, respectively. An energy diagram was proposed to explain the PL procedure. The electronic states of the hump serve as a trap for UV-excited electrons, and those of the lower energy pre-edge peak act as a color center for the self-activated titanate phosphors. We believe that the energy diagram proposed in this study will provide new insights into the development of high-efficiency rare-earth-free phosphors.

4 Investigation of local distortion of TiO_6 octahedron in $SrTiO_3$ with UV irradiation by EXAFS

4.1 Experimental setup and Configuration

The EXAFS experiments were performed in the beamline 12C of the PF. The spectra were measured in the transmission mode at 22 K (the lowest temperature available on the beamline) to 300 K. To accommodate the effective penetration depths of UV and X-ray radiation, the powder samples must be prepared with a sufficiently low thickness. Considering this, equivalent $SrTiO_3$ superfine powder was deposited on three Millipore membrane filters. During the EXAFS experiments, three Millipore membrane filters were paralleled in line receiving X-ray, and each of them was irradiated by UV light. A schematic of the $SrTiO_3$ sample setup is shown in Figure 4-1. The obtained sample thickness corresponded to an absorption jump $\Delta\mu$=0.7 at the Ti K-edge. An optical fiber with three furcated ends was used to meet the number of membranes.

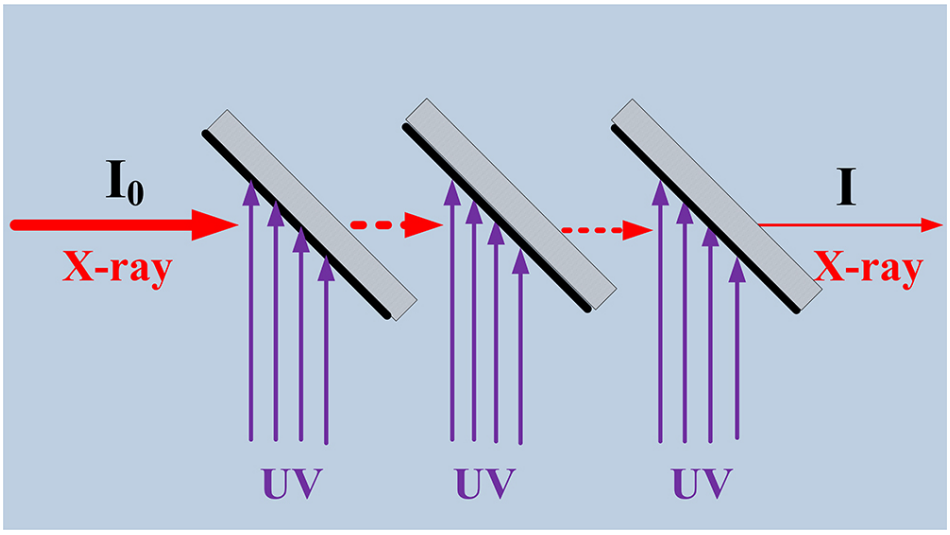

Figure 4-1: Schematic diagram of $SrTiO_3$ sample setup

Generally, a temperature gradient exists between the sample and the temperature sensor, which causes experimental errors in terms of temperature. To ensure the consistency of temperature between the sample and the thermal sensor, the membranes were sandwiched in a good heat conductor (copper) with an opening hole for receiving X-rays (inset of Figure 4-2). Low temperature XAS measurements were performed at 22–300 K using a closed-loop liquid helium cryostat with a heating resistor.

The beamline stage setup is the same as that in the XANES experiment described in section 3. To facilitate UV light irradiation on the chamber, one side of the Kapton film window was replaced with SiO_2 glass (Figure 4-2).

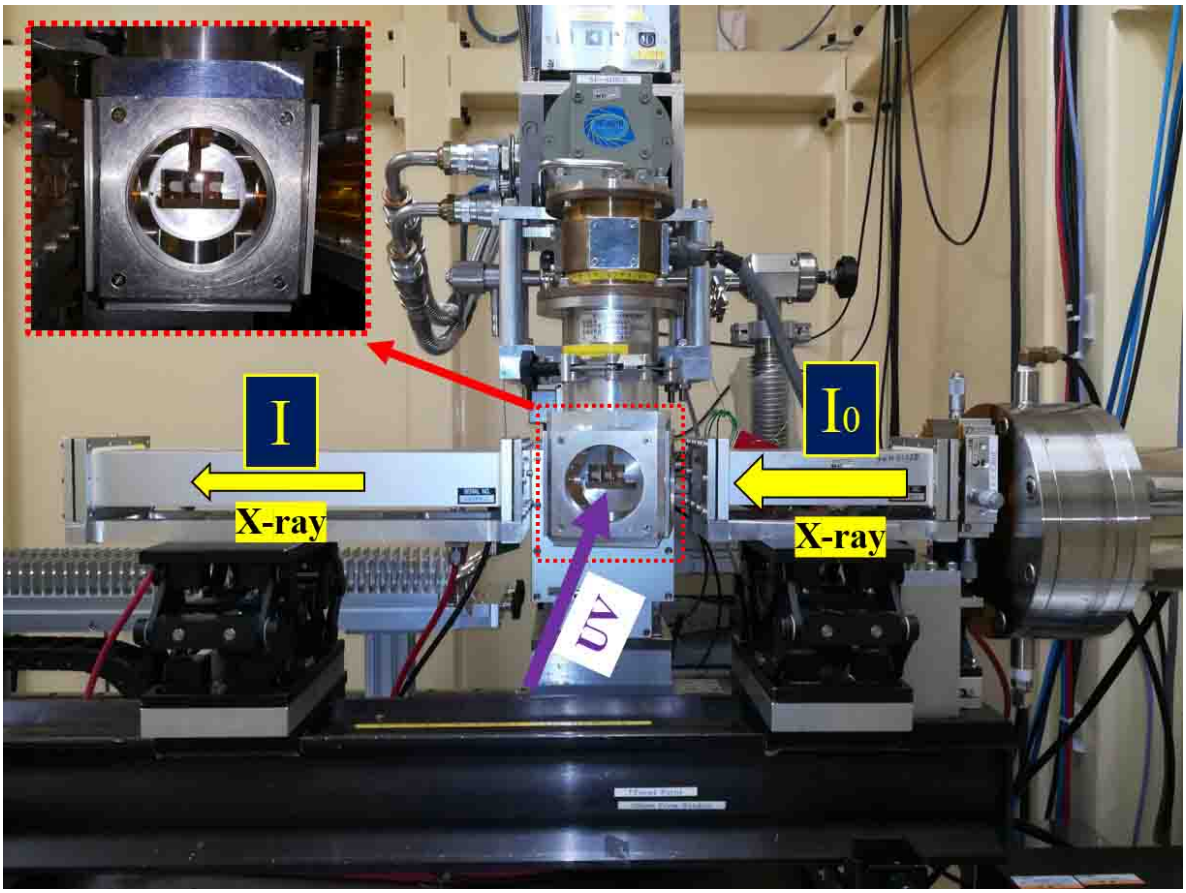

Figure 4-2: Schematic of the EXAFS experimental setup of BL-12C at the Photon Factory.

4.2 XAS of $SrTiO_3$

The normalized $SrTiO_3$ Ti K-edge XAS data at 22 K are shown in Figure 4-3; the detailed procedure of normalization was explained in the experimental section. The main edge is caused by the Ti 1s-4p dipole transition. The inset in Figure 4-3 shows the pre-edge feature of $SrTiO_3$ Ti K-edge XAS. The first two small peaks in the pre-edge region are caused by the 1s-3d quadrupole transition. The interpretation of the pre-edge peaks of Ti K XANES is already shown in section 1.2. Previous studies have reported that the intensity of e_g is related to the Ti ion displacements [55, 61]. Specifically, Nakajima investigated the UV-induced one-dimensional vibration of Ti ions in $SrTiO_3$ [62]. Because the XANES is very sensitive too the local structure environment. Once there is Ti ion displacement along the z direction, the hybridization of $3d_{3z^2-r^2}$ and $4p$ will be enhanced, resulting the variation of the eg peak in the pre-edge region. The post edge that contains the EXAFS oscillation has not been comprehensively studied under UV irradiation, because controlling the penetration of UV light and X-rays is difficult. In this study, superfine $SrTiO_3$ powder was used to improve the UV effect.

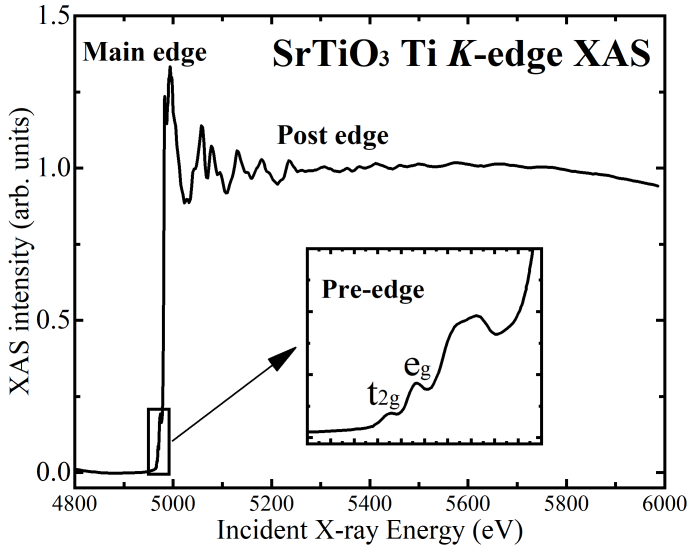

Figure 4-3: Normalized Ti K-edge XAS of $SrTiO_3$ at 22 K

4.3 EXAFS Data fitting

As discussed in section 1, the purpose of studying $SrTiO_3$ in this thesis is to analyze the local structure of $SrTiO_3$ and the variation of the local structure under UV irradiation. To extract structural information from the EXAFS oscillation, the starting structure model of $SrTiO_3$ must be built, and the scattering paths used to fit the EXAFS oscillation must be calculated by FEFF. Although the well-known structures of $SrTiO_3$ are cubic (P3m3) and tetragonal (I4/mcm), these results give only the macroscopic structure of $SrTiO_3$ based on the results of XRD. The structure in the microscopic scale is quite different from that in the macroscopic scale, which has already been widely observed in many perovskite materials such as $BaTiO_3$ and $PbTiO_3$ [6, 63].

The background subtractions of the raw XAFS data were performed using the AUTOBK algorithm, which is embedded in the Athena software [64]. In the post edge, not all the frequencies belong to the oscillation of EXAFS; low frequency corresponds to non-structural Fourier components of the background signal. Thus, the ⟨Rbkg⟩ parameter was set to 0.6 to reduce the low-frequency Fourier components of the background signal. The normalization and background removal parameters are shown in Table 4-1.

Table 4-1: Normalization and background removal parameters used in the EXAFS data extraction.

Edge	E_0	Rbkg	Normalization order
Ti K	4978	0.6	3

During the fitting procedure, three structure model are tested: cubic, tetragonal, and rhombohedral. After comparing the fitting results, the tetragonal model gave the best statistical fitting results. So the structure model used in this study was a tetragonal model based on the results of the experiments of total neutron scattering [65]. The lattice parameter used in the FEFF calculation is shown in Table 4-2. It is well-known that the property of these calculated scattering paths highly depends on the symmetry of the crystal structure.

Table 4-2: The lattice parameter of $SrTiO_3$ used in the FEFF calculation.

Crystal System	Tetragonal		
Space Group	P4mm		
Cell parameters	a=3.905Å	c=3.93819Å	
Atom	x	y	z
Sr	0.00000	0.00000	0.00000
Ti	0.50000	0.50000	0.50025
O1	0.50000	0.50000	0.00000
O2	0.50000	0.00000	0.50000

In this study, the investigation of the location property of Ti along the z-axis is important. The atom position z of Ti set at 0.50025 corresponded to the Ti displacement along the z-axis with a value of 0.001Å (figure 4-4). The purpose of setting Ti displacement to this small value is to produce all the scattering paths required for the fitting procedure with the tetragonal model. During the fitting procedure, a parameter zTi was assumed to obtain the real value of Ti displacement along the z-axis. The scattering amplitude $F_j(k)$ and phase shift $\psi_j(k)$ of each scattering path were calculated using the FEFF code (version 9.6) using the exchange-correlation Hedin-Lundqvist potential. The calculations were performed for a cluster of radius 9 Å and centered at the Ti atom. The calculations of the cluster potentials were performed via the muffin-tin self-consistent-field approximation using the radius value of 7 Å.

Generally, in the microscopic level, the Ti ion displacement in perovskite-type titanates has two preferable directions: (a) the [001] direction corresponding to the tetragonal $PbTiO_3$ [66, 67], and (b) the [111] direction corresponding to the rhombohedral $BaTiO_3$ [6]. In this thesis, the Ti displacement along the [001] direction is presented, mainly because we aim to confirm the Ti vibration along the [001] direction under UV irradiation, which has been reported by Nozawa [15, 42]. The main parameters used in the fitting of the tetragonal model are listed in Table 4-3. Because of the high correlation between ΔE_0 and the phase-related parameters, ΔE_0 was set to -5.2 eV based on the average value of the first run of fitting for all

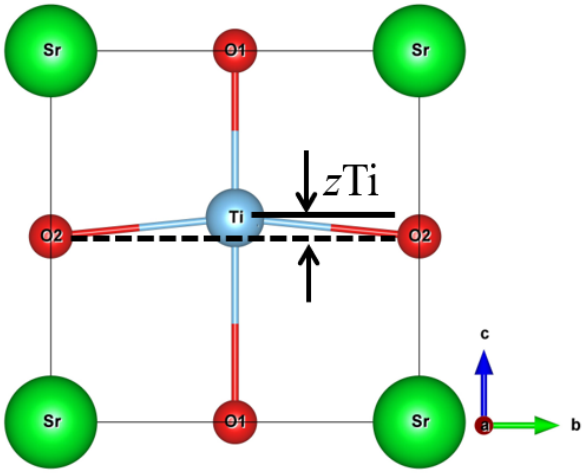

Figure 4-4: Crystal structure of $SrTiO_3$ used in the FEFF calculation. The Ti ion displacement with zTi=0.001 Å is indicated by an arrow.

Table 4-3: Main assumed parameters used in EXAFS data fitting with the tetragonal model.

Parameter	description	initial value
zTi	Ti ion displacement along [001] direction	0 Å
eta	Volumetric expansion coefficient for SS	0
etaMS	Volumetric expansion coefficient for MS	0
σ^2_{O}	MSRD of 6 O in the first shell	0.003
σ^2_{Sr}	MSRD of 8 Sr in the second shell	0.003
σ^2_{Ti}	MSRD of 6 Ti in the third shell	0.003
σ^2_{MS}	MSRD for the MS paths	0.003

data. Furthermore, the value of the amplitude reduction factor S_0^2 due to many-body effects was set to an estimated value of 0.95. The volumetric expansion coefficient *eta* was used due to the thermal expansion with the increasing temperature and the vibration of scattering atoms in the direction perpendicular to the chemical bonds. The actual distances from the central absorbing Ti atom to the scattering atom were the calculated atomic distance of the initial crystal structure and the deviation in the calculated atomic distance, which was caused by the Ti displacement and the volumetric expansion coefficient *eta*.

The k range used for the forward Fourier transformation is 2.0–14.5 $Å^{-1}$. The curve fitting was performed using the Fourier transform of the $k^2\chi(k)$ profile in the r space of 0.8–4.1 Å.

4.4 Temperature dependence of Ti K-edge EXAFS spectrum

Experimental k^2-weighted EXAFS profiles $k^2\chi(k)$ of $SrTiO_3$ at 22–300 K at the Ti K-edge are shown in Figure 4-5 (a). All the obtained EXAFS $k^2\chi(k)$ signals have a good signal-to-noise ratio. The signal stops at 15.5 $Å^{-1}$ because of the appearance of a small Cr K-edge, which is caused by a small Cr^{3+} contamination. The wave group from 3–9 $Å^{-1}$ represents the interference of the outgoing photoelectron waves from the Ti atom and the scattering waves from the first shell of six O atoms. The wave group from 9 $Å^{-1}$ to the end of this data represents the interference of the outgoing photoelectron waves from the Ti atom and the scattering waves from the second shell of eight Sr atoms and the third shell of six Ti atoms. Thus, each wave group contains the information about a specific structure. A clear trend of these oscillations is the decreasing intensity with the increasing temperature, which is due to the enhanced thermal vibration at high temperatures.

Figure 4-5 (b) displays the magnitude of the Fourier-transformed $k^2\chi(k)$ profiles |FT $k^2\chi(k)$|. The peak in the range of 1.0–2.0 $Å^{-1}$ corresponds to the six O atoms in the TiO_6 octahedral coordination. The two peaks in the range of 2.5–4.0 $Å^{-1}$, which are not well-separated, correspond to the eight Sr atoms in the corner of the cubic $SrTiO_3$ and the six Ti atoms at the center of the neighboring cubic $SrTiO_3$ units. It is noticeable that the intensity of all the peaks decrease with the increasing temperature. However, the decrease in

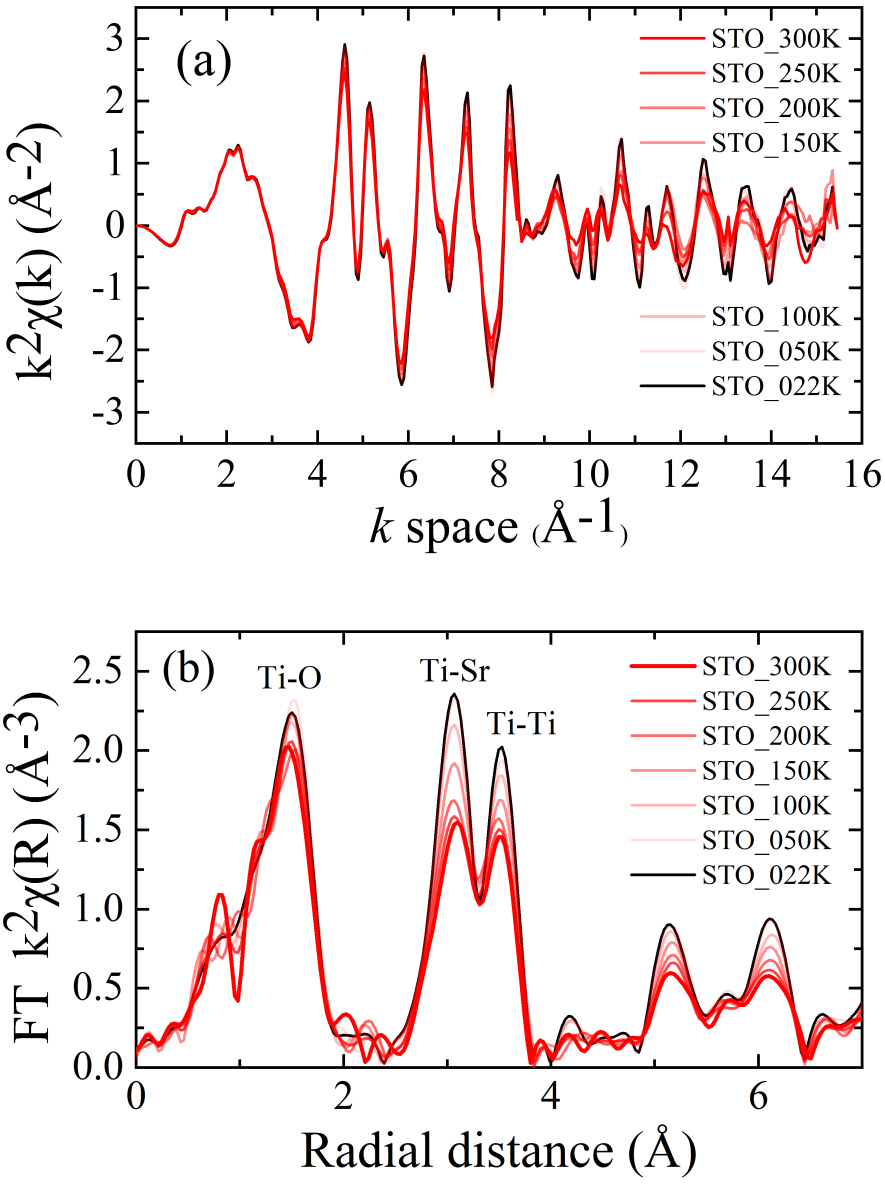

Figure 4-5: (a) k^2-weighted experimental EXAFS profiles $k^2\chi(k)$ of $SrTiO_3$ at the Ti K-edge, and (b) their Fourier transforms |FT $k^2\chi(k)$| from 22 K to 300 K.

the amplitude of the first peak is less than that of the second and third peaks, which can be explained by the bonding nature of Ti ions with the surrounding coordination. The chemical bond between Ti and O is a covalent bond, and Ti-Sr or Ti-Ti belongs to the ionic bond. Therefore, the TiO_6 octahedra can be considered to be relatively more rigid than the Ti-Ti and Ti-Sr sublattice [68].

Based on FEFF calculation, the obtained paths show that the first shell signal contains a single scattering from O coordination. The second peak contains a single scattering from Sr coordination and the triangle multiple scattering Ti_0-O-O-Ti_0 (Ti_0 is the absorber). The third peak contains a single scattering from Ti_0-Ti and various linear multiple scattering contributions with different Ti_0–O–Ti_0 chains.

Because the purpose of this work is to investigate the Ti ion motion, we mainly focus on the first shell. During the fitting process, the tails of the paths belonging to the second and third shells sometimes contribute to the first shell; thus, for obtaining a more accurate value, the second and third shells were also fitted. Analyzing the second and third peaks is more difficult because of the overlap of the contributions from outer coordination shells and strong multiple-scattering effects. The fitting of the data at 22 K using the tetragonal model is shown in Figure 4-6. The solid black line represents the experimental EXAFS profile, and the dashed red line represents the fitted profiles. The same parameter setting was used for all the data at different temperatures ranging from 22 K to 300 K. Each fitted profile agreed well with the corresponding experimental EXAFS profile. The misfit in the range of 0–0.9 Å was caused by the low-frequency background signal.

The effect of Ti ion displacement zTi along z-axis on temperature dependence is shown in Figure 4-7. Obvious Ti ion displacements are present over the entire temperature range. So the distortion of TiO_6 is confirmed by the results by using EXAFS. The origin of PL property can be explained with using the same electronic principle discussed in the last section with self-activated titanate phosphors.

The observed Ti ion displacements are contradictory to the centrosymmetric cubic and tetragonal structures obtained by XRD. As mentioned earlier, for a specific material, the

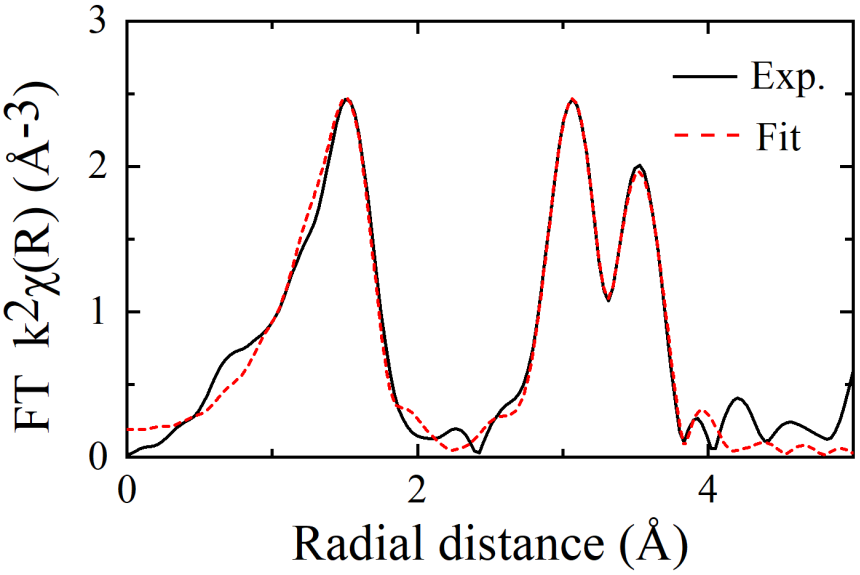

Figure 4-6: Magnitude of Fourier transforms |FT $k^2\chi(k)$| of Ti K-edge EXAFS of $SrTiO_3$ for experimental data (solid black line) and fitted data (red dashed line)

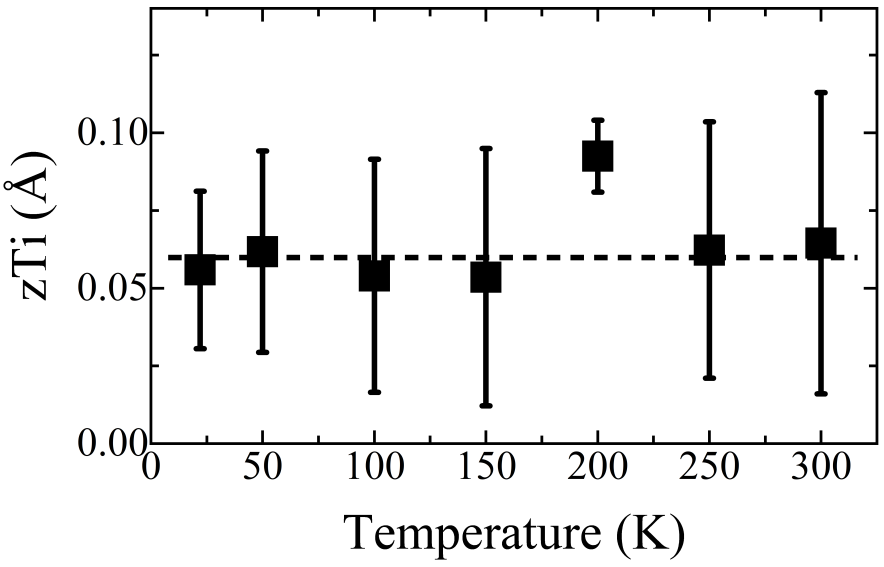

Figure 4-7: Ti ion displacement zTi along the z-axis, as measured by Ti K-edge EXAFS.

macroscopic structure obtained by XRD and the microscopic structure that can be measured by EXAFS are greatly different. The distinct Ti ion displacement was explained by the dynamic disorder by using nuclear magnetic resonance spectroscopy [38], which has been confirmed by many other reports as well [39, 40]. In addition, the measured Ti displacement explains the existence of the pre-edge feature in the Ti K-edge of $SrTiO_3$. Based on Vedrinskii's report, the area of peak e_g A in the pre-edge of Ti K-edge of $SrTiO_3$ is proportional to the square of the off-center displacement d [55].

$$A = \frac{\gamma}{3} d^2 \tag{4-1}$$

where γ is a constant [6]. If $SrTiO_3$ is perfectly centrosymmetric, the zero value of off-center displacement d cannot explain the pre-edge peak. However, in our obtained data, there are large error bars and irregular assumed values for zTi. This is caused by the high correlation between the parameter zTi and σ^2_{O}. The MSRD defined by $\left\langle (r - \overline{r})^2 \right\rangle$ indicates relative vibration between the absorber and scatter, which must be within a physically reasonable range of values. During the fitting procedure, the Ti ion displacement caused an uncertainty of statistical analysis. To obtain a physically reasonable value for each parameter, zTi was set to 0.06 Å; this value was not set arbitrarily. The dynamic disorder of Ti ions has an almost constant value, as indicated by EXAFS results [40]. σ^2_{O} with the temperature obtained after fixing zTi is shown in Figure 4-8. σ^2_{O} increased with the temperature, indicating that the variance in the distance between the absorber Ti_0 and the first shell O increased. The EXAFS equation indicates that $\chi(k)$ monotonically decreases with σ^2; therefore, the increasing σ^2_{O} with temperature explains the decreasing intensity of the EXAFS profiles $k^2\chi(k)$ and the first shell of |FT $k^2\chi(k)$|.

4.5 UV dependence of Ti K-edge EXAFS spectrum

The experimental k^2-weighted Ti K-edge EXAFS profiles $k^2\chi(k)$ of $SrTiO_3$ and the magnitude of their Fourier-transformed |FT $k^2\chi(k)$| at 22 K with and without UV irradiation are shown in Figure 4-9. It is noticeable that the intensity of both EXAFS profiles and their Fourier transforms are damped under UV irradiation. To clarify the reason for this damping,

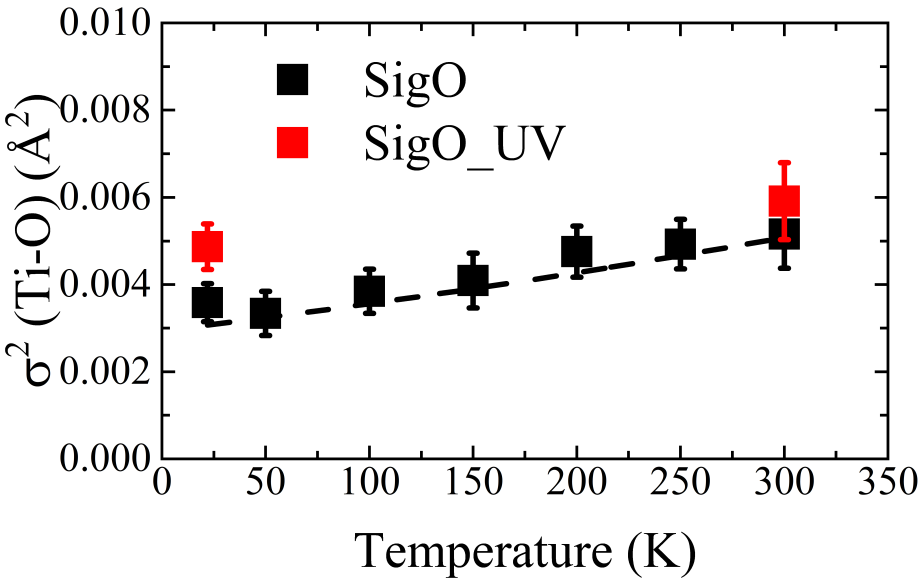

Figure 4-8: MSRD values obtained for Ti-O bond σ^2_{O} measured by Ti K-edge EXAFS with temperature dependence (black squares) and UV effect (red squares)

the fitting with the same parameter set was performed with UV irradiated data. The MSRD values obtained for UV irradiated data are compared with those of non-UV-irradiated data in Figure 4-8. It is apparent that the intensity damping in the EXAFS profiles with UV effect was caused by the increasing MSRD factor, which indicates the increasing variance of the distance between the Ti ion and O. However, one factor remains to be clarified. In the current fitting model, because the same MSRD factor σ^2_{O} was used for all the six O coordinations, the direction responsible for the increasing variance of the distance is unclear.

To find the specific direction that is sensitive to the UV effect, the six degenerate O were reduced to two vertical O (O11 and O12)and four planar O2 (Figure 4-4). Because of the relatively compensating distance between Ti-O11 and Ti-O12, they share the same MSRD factor σ^2_{O1}. For the planar O2, σ^2_{O2} is used. The results of fitting for σ^2_{O1} and σ^2_{O2} are shown in Figure 4-10. For the temperature effect, both σ^2_{O1} and σ^2_{O2} exhibit an increasing trend with temperature. For the UV effect, the error bar of σ^2_{O1} is large, which may be caused by the correlation with other parameters during the fitting process. The significant increase in the value of σ^2 for Ti-O11 is obvious, which indicates the relative movement between the Ti ion

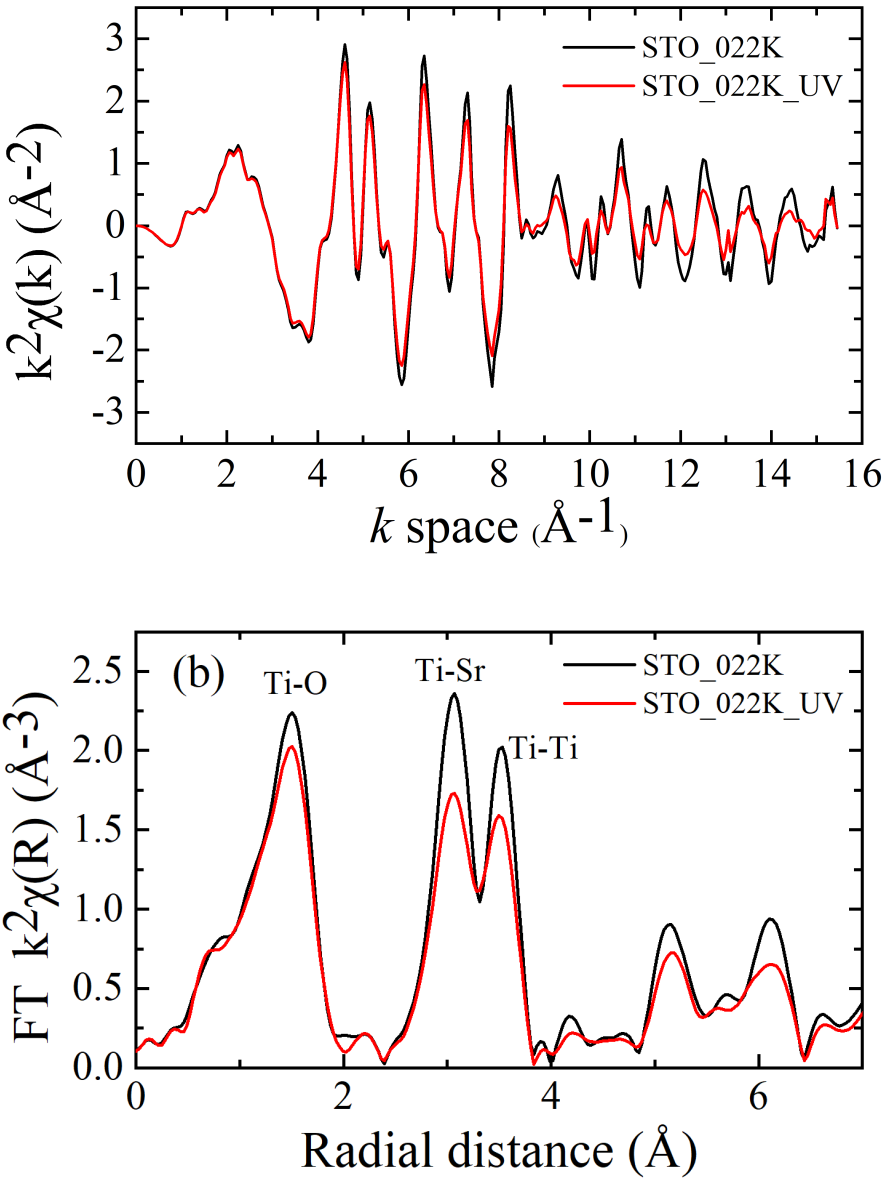

Figure 4-9: (a) k^2-weighted experimental EXAFS profiles $k^2\chi(k)$ of $SrTiO_3$ at the Ti K-edge, and (b) their Fourier transforms |FT $k^2\chi(k)$| at 22 K with and without UV irradiation.

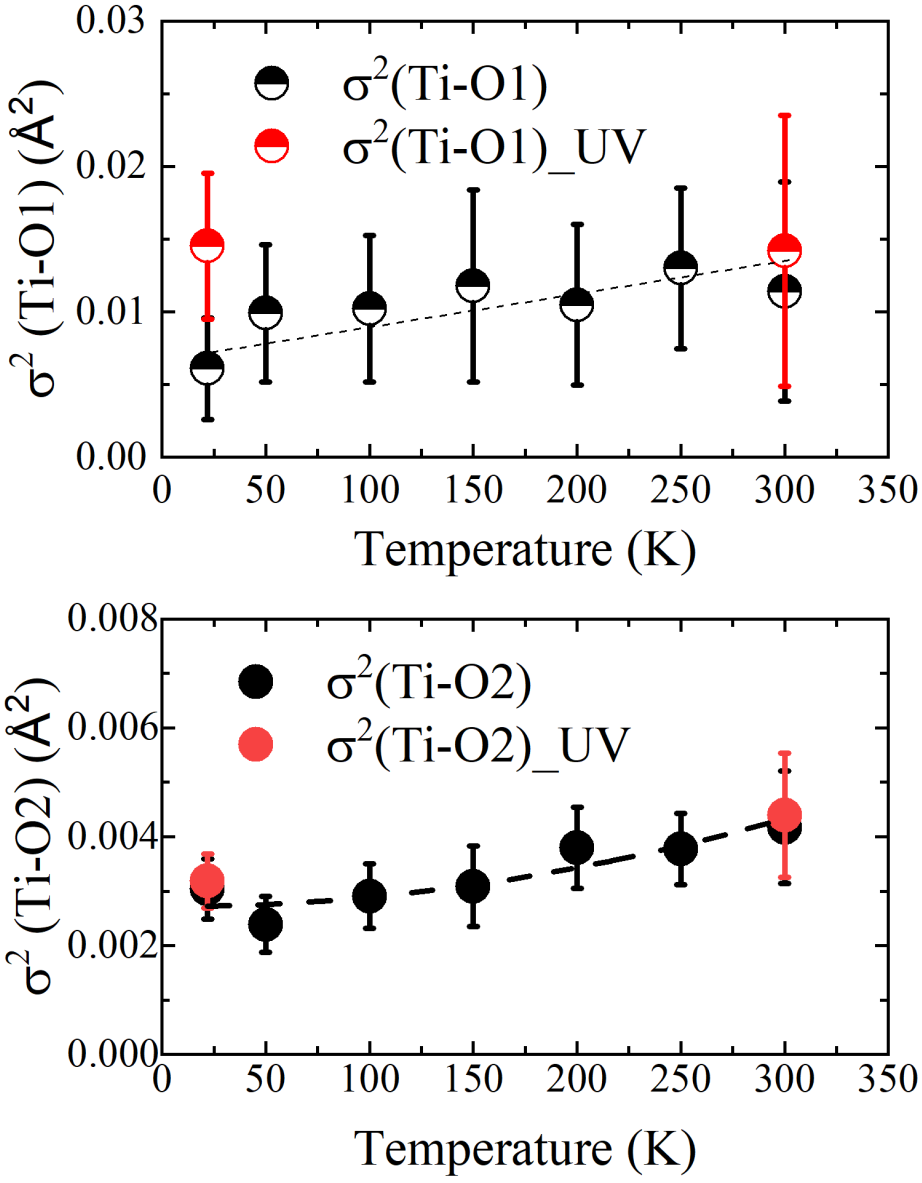

Figure 4-10: MSRD values obtained for Ti-O11 bond σ^2(Ti-O1) and (b) Ti-O2 bond σ^2(Ti-O2) measured by Ti K-edge EXAFS with temperature dependence (black markings) and UV effect (red markings)

and apical O. Under UV irradiation, σ^2_{O2} does not exhibit a clear increase in its value, and its variation trend with temperature is almost the same as that of the six degenerate O σ^2_O. This illustrates the relatively stable bond length between Ti and planar O. The variation of σ^2_{O1} and σ^2_{O2} under UV irradiation indicates the amplitude damping of the Ti K-edge EXAFS profiles $k^2\chi(k)$ of $SrTiO_3$, and its Fourier transforms are caused by the enhanced Ti ion vibration along the z-axis.

4.6 Conclusion

The local structure of $SrTiO_3$ based on the influence of temperature and UV irradiation was investigated using Ti K-edge EXAFS. The tetragonal structure model of $SrTiO_3$ with Ti ion displacement along the z-axis was used in the data fitting procedure. The amplitude of Ti K-edge EXAFS profiles $k^2\chi(k)$ of $SrTiO_3$ and the magnitude of its Fourier transforms |FT $k^2\chi(k)$| were damped with the increase in the temperature. The obtained increasing six degenerate MSRD of Ti-O bond σ^2_O illustrate that these dampings were caused by the enhanced thermal vibration. Clear Ti ion displacement was observed in $SrTiO_3$ for the entire temperature range, which explains the existence of the pre-edge peak of Ti K-edge XANES $SrTiO_3$. The amplitude of Ti K-edge EXAFS profiles $k^2\chi(k)$ of $SrTiO_3$ and the magnitude of its Fourier transforms |FT $k^2\chi(k)$| were also damped under UV irradiation. By reducing the degeneracy of six O in the TiO_6 octahedron to two vertical oxygen and four planar oxygen, a significant increase in the value of MSRD σ^2_{O1} and no increase in the value of MSRD σ^2_{O2} were obtained. This illustrates that the UV-induced damping of $k^2\chi(k)$ and |FT $k^2\chi(k)$| is caused by the enhanced Ti ion vibration along the z-axis.

5 Conclusions

In this research, two types of self-activated titanate phosphors were investigated, namely, fresnoite-type materials with TiO_5 polyhedron and perovskite titanate $SrTiO_3$ with TiO_6 octahedra. The electronic states of the fresnoite-type phosphors were analyzed by XANES to investigate the in-gap states, which are essential for realizing the PL property. The local structure of the TiO_6 octahedra in $SrTiO_3$ was analyzed by EXAFS to investigate the local structure for creating in-gap states. The UV irradiation and the temperature effect were considered in the experiments. The main results of this research are summarized below:

The Ti K-edge XANES of fresnoite self-activated titanate phosphors were analyzed under UV irradiation. The features in the pre-edge region were examined in detail to study the electronic states involved in generating the PL property. Theoretical calculations indicated that the observed large pre-edge peak corresponds to the electron transition from the Ti $1s$ core level to the electronic states hybridized with Ti $3d$, Ti $4p$, and O $2p$ states. The electronic states of the hump act as traps for the electrons excited by UV irradiation. The hybridization between Ti $3d$ and Ti $4p$ originated from the TiO_5 polyhedron. The electronic states of the large pre-edge peak provide in-gap states to emit visible light. It can thus be concluded that the TiO_5 polyhedra play an important role in self-activated titanate phosphors. An energy diagram of self-activated titanate phosphors was proposed to explain the electron transition in the PL process.

To investigate the relationship between the distortion of TiO_6 octahedron and the PL property, $SrTiO_3$ was chosen as the target material to study the local structure. The Ti K-edge EXAFS of $SrTiO_3$ was investigated at 22–300 K under UV irradiation. The EXAFS data were fitted well by using a tetragonal structure model with Ti ion displacement along the z-axis. Clear Ti ion displacement with 0.06 Å was obtained in $SrTiO_3$ over the entire temperature range. It not only confirmed the distortion of TiO_6 octahedron in $SrTiO_3$, but also explained the existence of pre-edge peaks in Ti K-edge XANES $SrTiO_3$. The Ti ion vibration along the z-axis in $SrTiO_3$ was significantly enhanced by UV irradiation. The increase in the intensity of Ti K pre-edge peak and the dielectric constant of $SrTiO_3$ under

UV irradiation is attributed to the enhanced Ti ion vibration.

In summary, the existence of TiO_5 polyhedron is essential to realize the PL property in non-ion-doped titanate compounds. The role of the TiO_5 polyhedron is to create in-gap states, which are required for emitting visible light. The TiO_5 polyhedron is intrinsically contained in fresnoite materials. The distortion of the TiO_6 octahedron in $SrTiO_3$ induces the PL property in $SrTiO_3$. The relationship between the PL property and the local structure distortion in non-ion-doped titanates opens up a new approach to characterize the titanium–oxygen polyhedron. Furthermore, the interaction between Ti ion vibration and UV-induced electronic transition in $SrTiO_3$ must be investigated to understand the cause of enhanced Ti ion vibration under UV irradiation, which will be the avenue of our future research.

Acknowledgment

My foremost and big "Thank you!" is to my mentor, Prof. Nobuo Nakajima, who was greatly patient in teaching me the areas of both daily life in Japan and scientific activities in lab. His guidance not only propelled me to gain a rich knowledge in physics, but also exposed to me the joy in scientific research, and has motivated me to take up research as a career. I would like to express my sincere gratitude to Dr. Naoki Ishimatsu, who offered valuable comments and suggestions for my research, as well as was concerned about my life. The most important thing I learned from them is the rigorous academic attitude, which has not only helped with my scientific research, but also enlightened me regarding my way of thinking and personal behavior in daily life. Their profound knowledge, keen scientific insight, and the spirit for exploring science will form an exemplary model for me that I will follow through my whole life.

I thank Prof. Yoshihiro Kuroiwa who provided me an opportunity to make an oral presentation in the Japan-Korea workshop, and provided many beneficial comments on my research. I thank all the staff of the Physical Science Office and the Student Support Office of the Graduate School of Science for helping me with paper works, information sharing, and scholarship recommendation. I would like to acknowledge the great support for the XAFS experiments from the beamline scientists in beamline 9A and 12C of Photon Factory. Their excellent instrumental operation helped us greatly with our experiment. I would like to greatly thank my colleague Doctor Andris Anspoks, who is from the Institute of Solid State Physics, University of Latvia. He provided me with invaluable help in the EXAFS data analysis.

I would like to thank all members of our laboratory: Mr. S. Ono, Mr. K. Ohshiro, Mr. Y. Noji, Mr. D. Miyashita, Mr. T. Toriyu, Mr. S. Kato, Ms. M. Kousa, and Mr. S. Iwasaki, Mr. A. Kumagae, Mr. K. Kuramochi, Mr. S. Kanamori, Mr. K. Hiromori, Mr. K. Ishimoto, Mr. Y. Kubo, Mr. H. Sakano, and Mr. Y. Endo. As an overseas student, with your help and friendship, I quickly adapted to the environment of learning and living in Japan, and maintained well with my research work. I greatly enjoyed getting along with you, and will never forget the happy times we worked and played together. I must thank Doctor Cong Lu,

who is a previous overseas student and another member of our laboratory, and coincidentally graduated from our lab by the time I arrived. He generously shared his experience with research in our lab and the life of staying in Japan.

I express my gratitude to the scholarship organizations JASSO and YAHATA for providing scholarships for my science works. I thank my best friends Yanning Wang and Jianye Sun very much. Exchanging scientific knowledge and experience with Yanning is something I enjoy doing. Since the times of high school up to the present, Jianye and I have always shared our thoughts about studying, growing, and the philosophy of human life. Every time I have been confused and depressed, he listened to my thoughts and encouraged me greatly.

To my father Baoyun Fan, mother Jinhui Li, brother Dongcan Fan, sister-in-law Shuyuan Song, my cutest nephew Songjia Fan, and niece Jiani Fan: I love you all very much. Although I was born in a farmer's family without adequate income and my parents have not received high levels of education, they have ever supported me with all their might and educated me through all these years. My brother Dongcan gave up his educational opportunity very early to make money to support our family. The birth of my nephew and niece has brought endless joy and pleasure to our family.

June 2020

Dongxiao Fan

References

[1] A. Fujishima and K. Honda, *Nature*, 1972, **238**, 37–38.

[2] Y. Kuroiwa, S. Aoyagi, A. Sawada, J. Harada, E. Nishibori, M. Takata and M. Sakata, *Physical Review Letters*, 2001, **87**, 217601.

[3] J. Ding, Y. Li, Q. Wu, Q. Long, Y. Wang and Y. Wang, *RSC Advances*, 2016, **6**, 8605–8611.

[4] J. M. Edge, Y. Kedem, U. Aschauer, N. A. Spaldin and A. V. Balatsky, *Physical Review Letters*, 2015, **115**, 247002.

[5] C. C. Sun, *Journal of Pharmaceutical Sciences*, 2009, **98**, 1671–1687.

[6] B. Ravel, E. Stern, R. Vedrinskii and V. Kraizman, *Ferroelectrics*, 1998, **206**, 407–430.

[7] J. J. Manappallil, *Basic dental materials*, JP Medical Ltd, 2015.

[8] S. Calvin, *XAFS for Everyone*, CRC press, 2013.

[9] G. Bunker, *Introduction to XAFS: a practical guide to X-ray absorption fine structure spectroscopy*, Cambridge University Press, 2010.

[10] A. J. McSloy, I. Trussov, A. Jarvis, D. J. Cooke, P. R. Slater and P. M. Panchmatia, *The Journal of Physical Chemistry C*, 2018, **122**, 1061–1069.

[11] J. Gopalakrishnan, K. Ramesha, K. K. Rangan and S. Pandey, *Journal of Solid State Chemistry*, 1999, **148**, 75–80.

[12] S. Sugano, *Multiplets of transition-metal ions in crystals*, Elsevier, 2012.

[13] P. Pizani, E. Leite, F. Pontes, E. Paris, J. Rangel, E. Lee, E. Longo, P. Delega and J. A. Varela, *Applied Physics Letters*, 2000, **77**, 824–826.

[14] S. Mochizuki, F. Fujishiro and S. Minami, *Journal of Physics: Condensed Matter*, 2005, **17**, 923.

[15] S. Nozawa, T. Iwazumi and H. Osawa, *Physical Review B*, 2005, **72**, 121101.

[16] Y. Li, M. Gecevicius and J. Qiu, *Chemical Society Reviews*, 2016, **45**, 2090–2136.

[17] Y. Huang, T. Tsuboi and H. J. Seo, *Ceramics International*, 2013, **39**, 861–864.

[18] X. Liu and J. Qiu, *Chemical Society Reviews*, 2015, **44**, 8714–8746.

[19] D. Harrison, N. Melamed and E. Subbarao, *Journal of the Electrochemical Society*, 1963, **110**, 23–28.

[20] E. Orhan, J. A. Varela, A. Zenatti, M. Gurgel, F. Pontes, E. Leite, E. Longo, P. Pizani, A. Beltran and J. Andres, *Physical Review B*, 2005, **71**, 085113.

[21] J. Woicik, E. L. Shirley, C. Hellberg, K. Andersen, S. Sambasivan, D. Fischer, B. Chapman, E. Stern, P. Ryan, D. Ederer *et al.*, *Physical Review B*, 2007, **75**, 140103.

[22] G. Blasse, *Journal of Inorganic and Nuclear Chemistry*, 1979, **41**, 639–641.

[23] Z.-y. Mao and Y.-c. Zhu, *Materials Research Bulletin*, 2014, **51**, 197–201.

[24] D. Fan, N. Nakajima and S. Kato, *Journal of Physics: Condensed Matter*, 2020.

[25] T. Hasegawa, S. W. Kim, S. Kamei, T. Ishigaki, K. Uematsu, K. Ohmi, K. Toda and M. Sato, *Dalton Transactions*, 2016, **45**, 11554–11559.

[26] B. Bouma and G. Blasse, *Journal of Physics and Chemistry of Solids*, 1995, **56**, 261–265.

[27] Q. Wu and Z. Hu, *Journal of the American Ceramic Society*, 2019, **102**, 2727–2736.

[28] P. Fleury, J. Scott and J. Worlock, *Physical Review Letters*, 1968, **21**, 16.

[29] H. Ohta, S. Kim, Y. Mune, T. Mizoguchi, K. Nomura, S. Ohta, T. Nomura, Y. Nakanishi, Y. Ikuhara, M. Hirano *et al.*, *Nature Materials*, 2007, **6**, 129–134.

[30] K. Ahadi, L. Galletti, Y. Li, S. Salmani-Rezaie, W. Wu and S. Stemmer, *Science Advances*, 2019, **5**, eaaw0120.

[31] J. Hemberger, M. Nicklas, R. Viana, P. Lunkenheimer, A. Loidl and R. Böhmer, *Journal of Physics: Condensed Matter*, 1996, **8**, 4673.

[32] U. Aschauer and N. A. Spaldin, *Journal of Physics: Condensed Matter*, 2014, **26**, 122203.

[33] V. Lemanov, E. Smirnova, P. Syrnikov and E. Tarakanov, *Physical Review B*, 1996, **54**, 3151.

[34] M. Itoh, R. Wang, Y. Inaguma, T. Yamaguchi, Y. Shan and T. Nakamura, *Physical Review Letters*, 1999, **82**, 3540.

[35] P. Zubko, G. Catalan, A. Buckley, P. Welche and J. Scott, *Physical Review Letters*, 2007, **99**, 167601.

[36] D. Lee, H. Lu, Y. Gu, S.-Y. Choi, S.-D. Li, S. Ryu, T. Paudel, K. Song, E. Mikheev, S. Lee *et al.*, *Science*, 2015, **349**, 1314–1317.

[37] X. Li, T. Qiu, J. Zhang, E. Baldini, J. Lu, A. M. Rappe and K. A. Nelson, *Science*, 2019, **364**, 1079–1082.

[38] B. Zalar, A. Lebar, J. Seliger, R. Blinc, V. V. Laguta and M. Itoh, *Physical Review B*, 2005, **71**, 064107.

[39] A. I. Frenkel, D. Ehre, V. Lyahovitskaya, L. Kanner, E. Wachtel and I. Lubomirsky, *Physical Review Letters*, 2007, **99**, 215502.

[40] A. Kodre, I. Arčon, J. P. Gomilšek and B. Zalar, AIP Conference Proceedings, 2007, pp. 481–483.

[41] M. Takesada, T. Yagi, M. Itoh and S.-y. Koshihara, *Journal of the Physical Society of Japan*, 2003, **72**, 37–40.

[42] S. Nozawa, T. Iwazumi, H. Osawa and T. Uozumi, *Applied Physics Express*, 2013, **6**, 061501.

[43] P. B. MOORE and S. J. Louisnathan, *Zeitschrift für Kristallographie-Crystalline Materials*, 1969, **130**, 438–448.

[44] T. Höche, W. Neumann, S. Esmaeilzadeh, R. Uecker, M. Lentzen and C. Rüssel, *Journal of Solid State Chemistry*, 2002, **166**, 15–23.

[45] P. Willmott, *An introduction to synchrotron radiation: techniques and applications*, John Wiley & Sons, 2019.

[46] M. Benfatto and C. Meneghini, *Synchrotron Radiation*, Springer, 2015, pp. 213–240.

[47] M. Nomura and A. Koyama, *Design and performance of a new XAFS beamline at the photon factory; BL-12C*, National lab. for high energy physics technical report, 1996.

[48] M. Newville, *Reviews in Mineralogy and Geochemistry*, 2014, **78**, 33–74.

[49] O. Bunău and Y. Joly, *Journal of Physics: Condensed Matter*, 2009, **21**, 345501.

[50] J. A. Van Bokhoven and C. Lamberti, *X-ray absorption and X-ray emission spectroscopy: theory and applications*, John Wiley & Sons, 2016, vol. 1.

[51] J. J. Rehr, J. J. Kas, F. D. Vila, M. P. Prange and K. Jorissen, *Physical Chemistry Chemical Physics*, 2010, **12**, 5503–5513.

[52] B. Ravel and M. Newville, *Journal of Synchrotron Radiation*, 2005, **12**, 537–541.

[53] M. Newville, *Journal of Synchrotron Radiation*, 2001, **8**, 322–324.

[54] E. Stern, M. Newville, B. Ravel, Y. Yacoby and D. Haskel, *Physica B*, 1995, **208**, 117–117.

[55] R. Vedrinskii, V. Kraizman, A. Novakovich, P. V. Demekhin and S. Urazhdin, *Journal of Physics: Condensed Matter*, 1998, **10**, 9561.

[56] F. Farges, G. E. Brown, J. Rehr *et al.*, *Physical Review B*, 1997, **56**, 1809.

[57] C. Lu, N. Nakajima and H. Maruyama, *Journal of Physics: Condensed Matter*, 2016, **29**, 045702.

[58] N. Nakajima, M. Deguchi, H. Maruyama, K. Ishiji and Y. Tezuka, *Japanese Journal of Applied Physics*, 2010, **49**, 09ME04.

[59] J.-H. Lee, W.-J. Lee, S.-H. Lee, S. M. Kim, S. Kim and H. M. Jang, *Physical Chemistry Chemical Physics*, 2015, **17**, 7857–7863.

[60] T. Learmonth, P. Glans, J. Guo, M. Greenblatt and K. Smith, *Journal of Physics: Condensed Matter*, 2009, **22**, 025504.

[61] M. Deguchi, N. Nakajima, K. Kawakami, N. Ishimatsu, H. Maruyama, C. Moriyoshi, Y. Kuroiwa, S. Nozawa, K. Ishiji and T. Iwazumi, *Physical Review B*, 2008, **78**, 073103.

[62] S. Kawakami, N. Nakajima, M. Nakatake, N. Kawamura, M. Mizumaki and H. Maruyama, *Japanese Journal of Applied Physics*, 2015, **54**, 10NC03.

[63] B. Ravel and E. Stern, *Physica B: Condensed Matter*, 1995, **208**, 316–318.

[64] M. Newville, P. Līviņš, s. Y. Yacoby, J. Rehr and E. Stern, *Physical Review B*, 1993, **47**, 14126.

[65] Q. Hui, M. G. Tucker, M. T. Dove, S. A. Wells and D. A. Keen, *Journal of Physics: Condensed Matter*, 2005, **17**, S111.

[66] N. Sicron, B. Ravel, Y. Yacoby, E. A. Stern, F. Dogan and J. J. Rehr, *Physical Review B*, 1994, **50**, 13168.

[67] B. Ravel, N. Slcron, Y. Yacoby, E. A. Stern, F. Dogan and J. J. Rehr, *Ferroelectrics*, 1995, **164**, 265–277.

[68] A. Anspoks, D. Bocharov, J. Purans, F. Rocca, A. Sarakovskis, V. Trepakov, A. Dejneka and M. Itoh, *Physica Scripta*, 2014, **89**, 044002.